Sand production simulation under true-triaxial stress conditions

Younessi, A.[a], Rasouli, V.[a], Wu, B.[b]

[a] Department of Petroleum Engineering, Curtin University, Perth, Australia

[b] CSIRO, Division of Earth Science and Resource Engineering, Melbourne, Australia

Abstract

Laboratory sanding experiments were carried out under true-triaxial stress conditions. The objective was to investigate the effect of state of stresses and fluid flow on the mechanism of sanding, and the development of the failure zone around the borehole. The experiments were conducted on 100×100×100 mm^3 cubic samples of synthetic sandstones. The samples were prepared based on an established procedure developed to produce weakly consolidated sandstone samples with identical physico-mechanical properties. The properties of the synthetic sandstone samples were determined by conducting a series of standard rock mechanics tests on cylindrical plugs. Using a true-triaxial stress cell (TTSC), cubic samples were subjected to true-triaxial stresses and radial fluid flow from the outer boundaries. The fluid flows through the sample radially and discharges from a hole drilled at the centre of the sample: this allows studying sanding initiation by changing the state of stresses, sample material and fluid properties. In this paper, firstly, the experiment equipment, setup and procedure are explained in detail. This is followed by presenting the results of two sets of experiments performed at two different states of stress. The maximum and intermediate principal stresses were applied laterally in both cases while the effect of changing the lateral stresses on the development of the failure zone around borehole was monitored. It was observed that the geometry (i.e. width and depth) of the failure zone developed around the borehole is a function of the lateral stresses ratio (i.e. lateral stress anisotropy). The experiments were also simulated numerically using ABAQUS in order to validate and interpret the results from the experiments. A good agreement was obtained between the results of both methods which confirm the importance of lateral stress anisotropy on the evolution of sanding. The observations and results of these experiments and numerical simulations will be presented and discussed.

Keywords:
Laboratory experiment
True-triaxial stress
Sand production
Borehole failure
Numerical modelling

1 Introduction

Stability of underground excavations is a significant concern in the field of civil, mining and petroleum engineering. In the petroleum engineering, formation failure around a borehole may cause severe problems in different stages of drilling and production. Amongst the problems is failure of borehole in sandstone reservoirs during hydrocarbon production, known as "sand production". Sand production not only causes several problems in maintaining borehole integrity but also is a problem during production where erosion induced damage to the downhole and surface production facilities is likely to occur.

The majority of sand production problems occur in unconsolidated sands. In this type of formation the bonds between the sand grains are extremely weak, and borehole stability is mainly governed by the sand-arch formed around the borehole [1-5]. Sand production is also observed in weakly consolidated sandstones where sand production initiates due to stress induced failure of the sandstone in the vicinity of the borehole [6, 7]. Once sandstone is in a state of failure, fluid flow applies a drag force to the sandstone resulting in some of the sand grains to detach from the wellbore wall and fall into the wellbore. In cased holes sand production is through the perforation tunnels but the mechanism (i.e. failure of sand formation and transportation of sand grains by the means of fluid flow) remains the same.

Stress induced failure occurs when the stresses around the excavation exceed the rock strength [8]. In the context of geomechanics, the state of stresses around a single borehole is a function of three principal far-field stresses; usually a vertical and two horizontal stress components. Different modes of failure have been observed around a circular opening. These modes of failure have been classified with respect to the state of stresses in vicinity of the borehole [9, 10]. Figure 1 shows the main failure modes around a borehole with isotropic and anisotropic stresses perpendicular to the borehole axis. It should be noted that rock mechanical properties (stiffness and brittleness) and rock anisotropy (e.g. lamination) also affect the deformation and failure of cavity [11, 12].

Failure mode **A**, shown in Figure 1, is the most commonly observed failure mode around a borehole [13], w) is the maximum stress, the radial stress (σ_r) is the minimum stress, and the axial stress (σ_a) is the intermediate stress ($\sigma_\theta > \sigma_a > \sigma_r$).

It is more convenient to conduct experiments under isotropic stress conditions on cylindrical samples than under true-triaxial stress conditions [12-15]. This is due to the fact that sample preparation and equipment setup are easier for a cylindrical sample than for a rectangular prism sample which is required in true-triaxial tests. In this type of experiment the isotropic boundary

stresses lead to axisymmetric stress condition around the borehole. Nevertheless, the effect of the intermediate stress (axial) can be studied in vicinity of the borehole wall [13, 14].

A more realistic experiment should be the one which includes the effect of three independent stress components. In practice, this is only possible if the experiment is conducted on rectangular prism samples. In this approach, the boundary stresses represent three principal far-field stresses, and the induced stresses around the borehole are not symmetric. Few experiments have been conducted under true-triaxial stress conditions to study borehole failure [16-19].

The key difference between sand production and borehole failure laboratory experiments is the presence of fluid flow through the sample and borehole during the tests. This has been done several times in cylindrical shape sample [20-25], but very few attempts have been done to simulate sanding in true-triaxial boundary stress condition [26, 27].

The main objectives of this study were to investigate the sanding mechanism under true-triaxial stress conditions and fluid flow, and to investigate the dimension of failure zone developed around a single borehole due to sand production. This has been done by introducing a new experimental setup and procedure to simulate sand production in a single borehole under true-triaxial stress and fluid flow conditions. The mechanism of sand production was studied experimentally to understand the impact of stresses and fluid flow on failure around borehole. The geometry of the failed zone due to sand production was investigated at the end of the experiments. The findings were validated and interpreted by simulating the experiments using a finite element method program (here was ABAQUS). In the following sections the procedure to conduct the experimental and numerical simulations will be described in detail.

2 Experimental simulation

The sand production experiments were conducted using a true-triaxial stress cell (TTSC). The TTSC was designed for conducting advanced geomechanical laboratory experiments under true-triaxial state of stresses [28]. In this study, for the first time the TTSC was used for sand production simulation. In the following sections the properties of the samples used in these tests and the experiment setup and procedure are described in detail.

2.1 Sample preparation and properties

Synthetic sandstones were previously used to simulate sand production and borehole failure in weakly consolidated sandstone [7, 25, 27]. Although it is preferable to conduct the tests on samples of natural sandstones, this is subjected to some limitations. Firstly, it is practically impossible to collect an intact sample of weakly consolidated sandstone with sufficiently large dimension from downhole. Secondly, the physico-mechanical properties of rocks taken from

outcrop (even if they are representative for downhole sandstones) may not be homogeneous while it is possible to make synthetic samples with reasonably homogeneous properties [7].

Sophisticated methods have been proposed to generate realistic synthetic samples [29]. To obtain a sample suitable for this purpose it is important to establish a consistent sample preparation procedure. In addition, prior to the sanding experiment, a series of conventional rock mechanical tests need to be carried out to obtain the physico-mechanical properties of the synthetic rocks. The details of sample preparation and a review of the equipment used for this purpose were reported previously by the Authors [30]. This procedure was used to make all samples used for the experiments in this study.

Synthetic sandstones are basically composed of sands, cement and water. Mechanical properties of the produced sample are a function of the ratio of the individual components used in the mixture. It has been observed that a small variation in the component ratio during sample preparation could result in a significant change in the properties of the final product. This indicates the importance of careful selection of the basic components.

The size of the grains selected for sample preparation depends solely on the purpose of the undergoing study. The grain size was selected to be 200-850 μm for the current study, and chemical analysis shows that the sand grains are 99.6% of silica. Synthetic sandstones with different ratios of sand, Portland cement and water were produced and tested to obtain samples with desirable characteristics for sanding experiments. The proposed mixture was similar to what was proposed in reference [31], which consisted of sand-cement and water-cement weight ratio of 10 and 1.25, respectively.

Samples used for sand production experiments were 100×100×100 mm^3 cubes. These samples were casted in standard concrete moulds. The cement was not strong enough to bond sand particles in the early stage of curing. Hence, the samples were left in the moulds for three days (the sample loses its integrity if taking it out of the mould earlier). The samples were then submerged into water and cured for 18 days. In order to reduce the effect of over-curing, the samples were dried in an oven at a temperature of 60°C for two days. Thereafter, to reduce the effect of weathering the samples were wrapped in plastic film and stored in a dry room environment.

The properties of the sample and the fluid used for laboratory experiments were measured by conducting a series of laboratory tests following ISRM suggested methods [32-35]. The results of the triaxial compressive tests were shown in Figure 2. The top graph in Figure 2 shows the axial stress-strain curves of the sample under different confining pressures. This figure shows that the sample behaves more ductile in higher confining pressures. This is probably due to low sand-cement ratio and/or the fact that the sample was cured under free stress environment. From the

stress-strain curves it appears that the confining pressure has negligible effect on the Young's modulus. The bottom graph in Figure 2 shows the failure envelope of the sample in σ_1-σ_3 space.

The physical and mechanical properties of the synthetic sandstone are tabulated in Table 1. The fluid properties of the oil used for sand production experiments are also given in this Table. A sample with properties close to those given in Table 1 may be considered as weakly consolidated sandstone. These types of sandstones are prone to sanding during production from a reservoir.

2.2 Experiment setup

The TTSC consists of a pressure cell surrounded by a vertical and four horizontal hydraulic rams (Figure 3). The maximum operating loads are 450 kN and 250 kN for vertical and horizontal rams, respectively. The cell can be pressurized up to 21 MPa to simulate pore pressure by injecting fluid. The TTSC can accommodate a cubic sample of up to 300×300×300 mm^3 size for conducting various advanced laboratory experiments under true-triaxial stress conditions. An outlet hole is designed at the bottom of the cell to access the sample during the test for injection purposes in hydraulic fracturing experiments or disposal of the produced fluid and sand grains in a sanding test.

As shown in Figure 3 the produced sand grains are collected in a graduated measurement tube connected to a T-junction below the pressure cell. A cylindrical screen was mounted inside the T-junction to separate sand grains from the produced fluid. The separated sand grains deposit into the measurement tube due to gravity force during the test.

The special design of the hydraulic rams allows their independent control using manual or automatic hydraulic pumps. In this study, the fluid flow, which simulates the hydrocarbon production, was injected into the cell via an inlet, using a reciprocating pump with a maximum flow rate of 130 lit/hr and a maximum pressure of 36 MPa. Figure 4 shows the configuration of the pumps and arrangement of flow lines used for doing a sanding experiment using the TTSC.

Before setting up the sample in the TTSC, a 15 mm diameter hole was drilled in the centre of the 100×100×100 mm^3 sample to represent a borehole. The dimension of the borehole was selected to minimise the effect of sample boundary on failure around the borehole. This was checked for theoretically prior to run the tests [36].

In order to accommodate a 100×100×100 mm^3 sample inside the TTSC the gap between the sample and platens must be filled. To do this, six Aluminium blocks of size 97×97×100 mm^3 were placed around the sample to transmit the loads from the platens to the sample surfaces. A gap was formed between the neighbouring spacers as a result of the spacer size being smaller than the sample size. These gaps serve two purposes: firstly, it accommodates the sample deformation due to loading, and secondly, it allows the injected fluids to flood the sample. The stress concentration, introduced by the difference between the areas of the sample and spacers, at the corner of the

sample is negligible (see Section 3.2). The upper and lower faces of the sample were sealed using a 1 mm thick rubber sheet glued to these faces to simulate a radial flow around the borehole. The lower sheet has a 15 mm diameter hole at its centre to connect the hole to the outlet of the pressure cell. The lower Aluminium spacer has the same diameter hole. To ensure that the fluid pressure is uniform at the boundary of the sample four woven stainless steel wire meshes were placed around the sample (Figure 5).

2.3 Experiment procedure

In a laboratory experiment, failure around a borehole is not only a function of rock properties and state of stresses but also depends on the loading path. This is due to the nonlinear behaviour of the sample material within the plastic zone. This suggests that depending on the purpose of the experiment, the loading path should be designed accordingly.

One may consider infinite loading paths to reach a specific state of stress. For instance, Figure 6 shows the results of two theoretical models under two different stress paths leading into the same final state of stresses. From this figure it can be seen that how different failure geometry and pattern could develop around the borehole under different loading paths. The top graph in Figure 6 shows that if the initial stresses are applied hydrostatically, the initial failure zone would be symmetrical. However, when stresses start deviating from hydrostatic, additional failure zone in breakout pattern may form around the borehole wall. The bottom graph in Figure 6 shows the case in which the stress ratios are maintained constant during the entire experiment. In this case rock failure may develop gradually with a breakout pattern around the borehole wall. The latter path is the most representative path to simulate the in situ stresses, which was also used in our experiments.

The experiments were conducted with specific stress ratios. During the experiments the stresses and pore pressure were increased in steps while their ratios were kept constant. This is because of the fact that it takes time to reach the condition of steady state fluid flow.

After the sample was placed inside the TTSC a consistent procedure was followed in all tests to apply the stresses. The procedure includes:

(*i*) Sample sealing: To ensure that the area between sample and the upper and lower spacers are perfectly sealed, an axial stress (vertical stress) of 1.4 MPa was applied to the sample.

(*ii*) Sample saturation: After applying the vertical stress, the sample was saturated by continuous flow of oil for at least 10 minutes until no air bulbs were observed in the fluid from the outlet.

(*iii*) Sand production: Stresses and fluid injection pressure were increased gradually in steps according to the stress ratios defined for the test. Each step lasted for at least 5 minutes.

(*iv*) Unloading: The unloading phase was similar but opposite to that of the preceding stage with shorter steps. This was done to ensure that the unloading stress path did not affect the geometry of the failure zone around the borehole.

Figure 7 shows a schematic of the loading-unloading path for a typical test conducted for sanding experiments (different stages are marked on the chart).

2.4 Experiment Results

Several preliminary tests were carried out to ensure that the experiment setup and procedure defined in the preceding sections apply correctly. The preliminary tests were terminated at different points in stage *iii* of the loading path and the failure around the borehole was characterized in a post-test measurement. This was done to have a better understating of the mechanism of the failure around the borehole. This information was used to design appropriate stress ratios and loading/unloading stages for the rest of the test program.

In the following sections the sanding mechanism observed in the preliminary tests (which was also observed in the main experiments) is explained in detail. Thereafter, the results of the main experiments will be presented and interpreted.

2.4.1 Sanding mechanism

Sanding was monitored by observing the produced sand grains collected in the measurement tube (described in Section 2.2). Since the borehole deformation was not monitored during the experiments, the yield point of the borehole could not be identified. The initiation of sanding was assumed to correspond with the observation of first sand grains in the measurement tube. Figure 8 shows the stress path and the amount of sand produced of one of the preliminary experiment (test number B1600). From this figure following conclusions can be drawn regarding failure and sanding mechanism:

(1) Based on the theoretical model, the material surrounding the borehole yielded at the very early stage of loading (at the beginning of stage *ii* in the loading path). However, the residual bond strength between the sand grains prevented the grains from being displaced and fell into the borehole. The drag force of fluid flow appears to be inadequate to wash out the failed sand material from the borehole wall.

(2) By increasing the stresses and pore pressure at boundaries, the dimension of the yielded zone around the borehole increased (the dimension of yield zone was estimated from numerical models in Section 3). Sand production was initiated once the boundary pore pressure increased up to 2 MP: this is when small amount of sand grains were observed in the measurement tube. The drawdown pressure at the onset of sanding is referred to *critical drawdown pressure* [37].

It should be noted that for the sample used in this study, the onset of sanding does not correspond to onset of yielding. Similar behaviour was observed in previous literatures [38].

(3) A relatively large amount of sand grains were produced when pore pressure reached 3.2 MPa. However, the rate of produced sand reduced after a certain period of time. The failed sand is partially removed as the remaining volume has some residual strength which allows them to be attached to the borehole wall. We refer to the drawdown pressure corresponding to this boundary pore pressure as *destructive drawdown pressure*.

(4) Eventually, increase in the boundary stresses and pore pressure resulted in progressive failure. A large amount of sands produced and discharged through the outlet tube. Consequently, a large outer boundary displacement in the direction of maximum lateral stress was observed. This was identified when the speed of the corresponding Automatic Pump, which applied the maximum lateral stress, was dramatically increased. The sand grains were produced continuously till the experiment was terminated. Large deformations were observed at the borehole wall after the sample was removed from the TTSC. This stage, where sand grains are produced continuously and the borehole wall does not stabilize, can be referred to *catastrophic* or *progressive sanding*. Theoretically, sanding is expected to be stabilized after a certain period of time. The fact that sanding was not stabilized in the experiments is due to the limited sample size and it may not be representative of real in situ behaviour.

Because the sample was totally failed by the end of loading stage, the test was terminated immediately without following the unloading procedure discussed in the preceding section. In the main experiments designed for this study, we only proceeded to stage 3 as the objective was to study the failure pattern and geometry of the failure zone around the borehole. The mechanism explained above is illustrated in Figure 9.

2.4.2 Geometry of the failed zone

To investigate the geometry (i.e. width and depth) of the failure zone in the main experiments, the sample was unloaded (as explained in Section 2.3) and removed from the TTSC. Large amount of failed sand grains were still attached to the borehole wall due to residual strength. These grains were detached from the borehole wall by blowing pressurized air. This was done under free stress state, so the cavity produced was not expand further. The shape of the failure zone was then captured precisely using a borescope (Figure 10). Table 2 summarizes the magnitudes of stresses and pore pressures applied to the boundary of the samples in each tests, as well as the dimension of the corresponding failure zone.

The results presented in Table 2 imply that in each set of experiments the depth of the failure zones was essentially unchanged. This suggests that the minimum lateral stress (σ_l) has

minor effect on the depth of failure zone for the condition that we studied. On the other hand, the average depth of failure zone in the two sets of experiments was quite different. The depth of failure zone in second set with maximum lateral stress (σ_L) of 16 MPa is larger than that of the first set of experiments. It may be postulated that the magnitude of the maximum lateral stress has a major impact on the depth of failure zone. However, this needs further investigations for other cases to draw a more generic conclusion.

The results presented in Table 2 also show a noticeable change in the width of the failure zone corresponding to different minimum lateral stresses. It is seen that by increasing the stress anisotropy, the width of the failure zone decreases: this means that the width of the failure zone is reversely proportional to the difference between the minimum and maximum lateral stresses. The latter observations confirm the results reported in literatures [18, 19].

For both sets of experiments, the results showed that in an anisotropic stress test the development of the failure zone was in the direction of minimum lateral stress, which is expected theoretically [39]. However, there was no preferred failure direction when the lateral stresses were isotropic. The main axis of wellbore ovalisation in the test with isotropic stresses was not oriented to a preferred direction but is mainly influenced by the heterogeneity of the sample.

These observations were theoretically supported when the experiments were simulated numerically using finite element method which is discussed in the next section.

3 Numerical modelling

The observations from the main experiments presented in the previous section were further investigated through the application of numerical simulations using ABAQUS. The analytical solutions for stresses around a borehole can be implemented to model the laboratory experiments to some extent. These models, however, are only available for plane-strain conditions where a plane section perpendicular to the borehole is modelled [8, 40, 41]. In a plane-strain model the out of plane stress (in this study the axial stress) is a function of in-plane stresses [42], which means that the out of plane stresses cannot change independently. Therefore, in order to study the stresses and failure (i.e. yield) around a borehole in true-triaxial stress conditions, a 3D model must be employed.

A 3D coupled numerical model was employed to simulate the sanding experiments. The geometry and input parameters for the numerical model are based on sample properties and experiment setup. These are discussed in more detail in the subsequent sections. The methodology used to numerically simulate the laboratory experiments in 3D is also explained. The results are discussed and compared to the laboratory observations.

3.1 Material properties

The material model which was used in the numerical modelling was defined based on the sample properties presented in Table 1 (see Section 2.1). A Drucker-Prager model with 0.8 flow stress ratio was found to be appropriate to model the synthetic sandstones (Figure 11). The results obtained from this model were found to have stronger correlation with the experimental results [36]. Previous investigations show that a Mohr-Coulomb model results in a greater failure dimension than the experimentally observed, and the failure dimension observed from an original Drucker-Prager model is significantly smaller than the experimental results [36].

A linear elastic-perfectly plastic constitutive model was assumed for the behaviour of the synthetic sandstone. The sample was assumed to deform linear elastically prior to yielding and perfect plastically after yielding. No strain hardening rule was assumed for the plastic model, i.e. yield function was assumed to coincide with the failure points. The plastic strain was not a concern in this study and therefore using any flow rule was acceptable. Thus, an associated plastic flow was presumed for ease of numerical modelling.

The fluid is assumed to be inviscid and incompressible. The flow regime in sand production laboratory experiments was assumed to be in steady-state condition. Finally, the pore fluid flow was assumed to be governed by the Darcy's law.

3.2 Modelling procedure

The geometry and boundary conditions of the numerical models were defined based on the sample geometry and experiment setup. A thick-section perpendicular to the borehole axis was selected for the analysis. Due to the symmetrical nature of the problem only a quarter of the section was modelled. This reduces the number of elements required for the model and therefore a less time for solution convergence. In contrary to the radial stresses that have a gradient along the lateral axis within the sample, the axial stress has no gradient along the vertical axis. Therefore, the axial dimension of the model can have any arbitrary dimension: in this study the model thickness was set to 10 mm.

The boundary conditions defined in the model must be representative of the loads and displacements applied to the boundary of the sample in the laboratory experiments. Uniform stresses were applied directly to the lateral boundaries. However, the vertical load was applied using a displacement boundary condition. The displacement corresponding to a specific stress was calculated from the Hook's law for elastic material. The normal displacement of the symmetric faces (i.e. the two lateral and the bottom faces) and their rotation components were fixed in the model. These symmetric faces with fixed displacements eliminated the rigid body motion.

The fluid flow is simulated by considering a uniform pore pressure distribution on the lateral outer boundaries of the sample and the borehole wall was treated as a free-drained surface. The upper and lower sides of the sample were set to be impermeable. Figure 12 shows the geometry of the 3D numerical model constructed for this study.

The Aluminium spacers were initially included in the numerical models. However, after comparing the results to a simpler case, where the boundary loads were directly applied to the sample, no significant differences were observed. Therefore, the Aluminium spacers were excluded from the numerical model and the loads were directly applied to the sample boundaries. In addition, the effect of stress concentration at the corners of the sample which was generated due to the difference of the sample area and the spacer effective area was investigated. The results indicated that the stress distribution close to the borehole was not affected by these stress concentrations.

A mesh sensitivity analysis was conducted to obtain the optimum number of elements for the numerical modelling [36]. Because there is no stress gradient in the axial direction only one element was considered along this dimension (see Figure 12).

3.3 Model validation

Plane-strain condition was considered as a special case of 3D model for validation purposes. As the axial load is applied through displacement, it is plausible to simulate a 3D model in plane-strain mode by setting the axial displacement to zero. Therefore, the model was validated against available 2D analytical solutions for a borehole under isotropic stress conditions [36]. Moreover, the stresses around a borehole in a cylindrical sample were compared to a cube sample. The results showed that the stresses are essentially identical except that slight deviation in the results was observed close to the outer boundaries. This observation implies that laboratory experiments can be conducted on cube samples with isotropic stresses to simulate a thick walled cylinder (TWC) test [43].

3.4 Modelling results

Using ABAQUS, 3D numerical modelling was performed to simulate the yield zones developed during testing synthetic samples in the laboratory. Width and depth of the failure zone are the two parameters to characterize the size of the failure zone. The results of the numerical models are shown in Figure 13 and Figure 14. For comparison purposes, the results of the experiments corresponding to these models are also plotted in these figures.

Figure 13 and 18 show a close agreement between numerical models and experimental observations. It must be noted that in the experiments, the yielded zone was assumed to be totally cleaned out by compressed air (see Section 2.4.2). These results show how experimental results

may be reproduced by the means of numerical simulations, the benefit of which is to do a large number of sensitivity analyses on different parameters.

3.5 Parametric study in effect of lateral stresses

The results presented in the preceding sections demonstrated the importance of the effect of lateral stress anisotropy on the characteristics of borehole failure. The presented results confirm partly the previous observations made by other researches, for instance those who reported the effect of lateral stress anisotropy on failure width [18, 19].

However, these results showed a different relationship between the depth of failure zone and lateral stresses. Previously, Haimson and Song (1993) showed that breakout depth increases as the minimum lateral stress was increased [19]. However in their experiments, the maximum lateral stress was not constant, and it was increased relatively with the minimum lateral stress.

In this study, it was observed that the depth of failure zone have more dependency to maximum lateral stress (σ_L) than the minimum lateral stress (σ_l). This was initially noticed through the laboratory experiments (Section 2.4.2) but was later verified by numerical models (Section 3.4). These findings were also observed when numerical models were run for different material models, such as Mohr-Coulomb and the original Drucker-Prager [36].

Although the numerical models presented in the preceding section shows the effect of σ_L on depth of failure to some extent, a new set of numerical simulations (hereafter referred to as set 3) was run to show this effect more explicitly. In set 3, σ_a a $_l$ were kept constant (8 MPa) w $_L$ was changed (8, 10, 12 and 14 MPa). Figure 15 shows the results of the numerical simulations of set 3 along with the results of set 1. It can be clearly seen that changes in σ_L has more effects on depth of failure than changes in σ_l.

In order to justify this observation, two different stages of failure were considered: initiation and stabilization of failure (Figure 16). For the ease of explanation only the maximum and minimum principal stresses in the vicinity of borehole will be considered to explain the failure mechanism. For the case of failure mode **A** (as was illustrated in Figure 1) these stresses are the tangential and radial stresses (σ_θ and σ_r).

The failure is initiated in the direction of σ_l at point a, where σ_θ is maximum ($\sigma_{\theta max}$) and σ_r is equal to borehole pressure (P_b). The magnitude of σ_θ in the direction σ_l (line A-A) when P_b=0 can be expressed as:

$$\sigma_{\theta\ \text{-A)}} = A\sigma_L + B\sigma_l ,$$

where, considering Kirsch's equations [8] for θ =0 we have:

$$A = \frac{1}{2}\left[2 + \frac{a^2}{r^2} + \frac{3a^4}{r^4}\right], \text{ and}$$

$$B = \frac{1}{2}\left[\frac{a^2}{r^2} - \frac{3a^4}{r^4}\right].$$

Figure 17 shows how parameters A and B vary along the radial distance from the borehole axis.

As anticipated, Figure 17 shows that A and B tends to become 1 and 0, respectively at distances further away from the borehole wall. This indicates that $\sigma_{\theta(A\text{-}A)}$ is independent from σ_l at far-field. The effect of σ_l on $\sigma_{\theta(A\text{-}A)}$ increases in the vicinity of the borehole. Yet, the contribution of σ_L to the magnitude of $\sigma_{\theta(A\text{-}A)}$ at the borehole wall is three times more than σ_l.

The borehole wall failure propagates along line A-A till the stresses at the tip of the failure are equal to the material strength (point b in Figure 16). During the failure propagation phase $\sigma_{r(A\text{-}A)}$ at the tip of failure is mainly governed by P_b and the residual strength in the yield zone. However, the magnitude of the $\sigma_{\theta(A\text{-}A)}$ is still a function of both σ_l a $_L$.

In order to understand the effect of lateral stresses on $\sigma_{\theta(A\text{-}A)}$ the stress profile along line A-A of the numerical models of set 1 and 3 were studied in more detail (Figure 18).

From Figure 18 it can be seen that the stress profile within the yield zone is independent of lateral stresses. Moreover as explained before, $\sigma_{r(A\text{-}A)}$ is independent from the lateral stresses at the elastic-plastic boundary (at the tip of failure, correspond to point b in Figure 16). Overall, it can be seen that beyond the tip of failure (i.e. in the elastic zone), $\sigma_{r(A\text{-}A)}$ is mainly governed by σ_l, while $\sigma_{\theta(A\text{-}A)}$ is mainly governed by σ_L. Hence, it is plausible to assume that the contributions of σ_l and σ_L on $\sigma_{\theta(A\text{-}A)}$ in the elastic zone beyond the tip of failure along line A-A are similar to Kirsch's equation.

To summarize, the above discussion demonstrated that the contribution of σ_L is more than that of σ_l on the magnitude of $\sigma_{\theta(A\text{-}A)}$, and $\sigma_{r(A\text{-}A)}$ at the failure tip is mainly governed by P_b and the residual strength in yield zone. Hence for a constant P_b the depth of failure, which is theoretically measured in the direction of A-A, is dependent more on σ_L than σ_l.

4 Conclusion

In this study two sets of experiments were conducted on identical cubic samples under different true-triaxial state of stresses to investigate the effect of lateral boundary stresses and fluid flow on borehole failure and sand production. The tests were carried out on 100×100×100 mm^3 synthetic sandstones. The test setup and procedure for a cubic sample subjected to true triaxial stresses and fluid flow was described in detail. The failure and sanding mechanism observed in the

experiments was discussed explicitly. Followings are a summary of the findings with respect to the sanding mechanism:

- Yielding of the borehole wall was not necessarily a direct indicator of sand production, as observed in our experiments. A minimum drawdown pressure was needed to induce sand production from the yield zone surrounding the borehole. This drawdown pressure was referred to as *critical drawdown pressure*.
- A large amount of sands could be produced when the drawdown pressure was sufficiently high and the yield zone was sufficiently large due to the loading of the sample. This drawdown pressure was referred to *destructive drawdown pressure.*
- When the entire sample yielded and the drawdown pressure exceeded the destructive drawdown pressure, continuous sanding with large deformation at the borehole wall was observed: this sanding mode was referred to *catastrophic* or *progressive sanding*. This is due to limited sample size and boundary effect and may not be representative of real in situ behaviour.

The failure geometry (i.e. width and depth) around the borehole were investigated experimentally and numerically. The following conclusions were obtained:

- The geometry of the failed zone around the borehole is directly related to the difference and magnitude of the far-field lateral stresses.
- The width of the failure zone is reversely proportional to the lateral stress anisotropy. The width of failure zone increases as the difference between the maximum and minimum lateral stresses decrease.
- The minimum lateral stress has a minor impact on the depth of failure zone around borehole. On the other hand, the extent of depth of failure zone was found to be mainly governed by maximum lateral stresses for a given material.
- As expected, the failures were developed in the direction of the minimum lateral stress. Also, the results showed that the direction of the failure zone under isotropic lateral stresses has an arbitrary direction which is mainly governed by heterogeneity of the sample.

References

[1] Morita N, Boyd PA. Typical sand production problems case studies and strategies for sand control. SPE Annual Technical Conference and Exhibition. Dallas, Texas; 1991.

[2] Hall CD, Harrisberger WH. Stability of sand arches: a key to sand control. J Pet Tech 1970; 22.

[3] Bratli RK, Risnes R. Stability and failure of sand arches. SPE J 1981; 21:236-48.

[4] Tippie DB, Kohlhaas CA. Effect of flow rate on stability of unconsolidated producing sands. Fall Meeting of the Society of Petroleum Engineers of AIME. Las Vegas, Nevada; 1973.

[5] Clearly MP, Melvan JJ, Kohlhaas CA. The effect of confining stress and fluid properties on arch stability in unconsolidated sands. SPE Annual Technical Conference and Exhibition. Las Vegas, Nevada; 1979.

[6] Geertsma J. Some rock-mechanical aspects of oil and gas well completions. SPE J 1985; 25:848-56.

[7] Perkins TK, Weingarten JS. Stability and failure of spherical cavities in unconsolidated sand and weakly consolidated rock. SPE Annual Technical Conference and Exhibition. Houston, Texas; 1988.

[8] Jaeger JC, Cook NGW, Zimmerman R. Fundamentals of rock mechanics. 4th ed: Wiley-Blackwell; 2007.

[9] Maury V. Observations, researches and recent results about failure mechanisms around single galleries. Report of the ISRM Commission on Failure mechanisms around underground excavations; 1987.

[10] Bratton T, Bornemann T, Li Q, Plumb D, Rasmus J, Krabbe H. Logging-while-drilling images for geomechanical, geological and petrophysical interpretations. SPWLA 40th Annual Logging Symposium; 1999.

[11] Tronvoll J, Fjær E. Experimental study of sand production from perforation cavities. Int J Rock Mech Min Sci & Geomech Abstr 1994; 31:393-410.

[12] Ewy RT, Cook NGW. Deformation and fracture around cylindrical openings in rock—I. Observations and analysis of deformations. Int J Rock Mech Min Sci & Geomech Abstr 1990; 27:387-407.

[13] Addis MA, Wu B. The role of the intermediate principal stress in wellbore stability studies: Evidence from hollow cylinder tests. Int J Rock Mech Min Sci & Geomech Abstr 1993; 30:1027-30.

[14] Lee DH, Juang CH, Lin HM. Yield surface of mu-san sandstone by hollow cylinder tests. Rock Mech Rock Eng 2002; 35:205-16.

[15] Santarelli FJ, Brown ET. Failure of three sedimentary rocks in triaxial and hollow cylinder compression tests. Int J Rock Mech Min Sci Geomech Abstr. 1989; 26:401-13.

[16] Mogi K. Deformation and fracture of rocks. Experimental Rock Mechanics: CRC Press; 2006.

[17] Lee M, Haimson B. Laboratory study of borehole breakouts in Lac du Bonnet granite: a case of extensile failure mechanism. Int J Rock Mech Min Sci & Geomech Abstr. 1993; 30:1039-45.

[18] Papamichos E, Tronvoll J, Skjærstein A, Unander TE. Hole stability of Red Wildmoor sandstone under anisotropic stresses and sand production criterion. J Pet Sci Eng 2010; 72:78-92.

[19] Haimson BC, Song I. Laboratory study of borehole breakouts in Cordova Cream: a case of shear failure mechanism. Int J Rock Mech Min Sci & Geomech Abstr 1993; 30:1047-56.

[20] Antheunis D, Fernandez Luque R, van der Vlis AC, Vriezen PB. The onset of sand influx from gas-producing friable sandstone formations - laboratory investigations. Society of Petroleum Engineers; 1979.

[21] Tronvoll J, Kessler N, Morita N, Fjær E, Santarelli FJ. The effect of anisotropic stress state on the stability of perforation cavities. Int J Rock Mech Min Sci & Geomech Abstr 1993; 30:1085-9.

[22] Khodaverdian M, Abou-Sayed AS, Ramos R, Guo Q, McLennan JD. Laboratory simulation of liner loading and near-wellbore permeability variation in poorly consolidated sandstones. SPE/ISRM Rock Mechanics in Petroleum Engineering. Trondheim, Norway; 1998.

[23] Papamichos E, Vardoulakis I, Tronvoll J, Skjærstein A. Volumetric sand production model and experiment. Int J Numer Anal Met Geomech. 2001; 25:789-808.

[24] Wu B, Tan CP. Sand Production Prediction of Gas Field - Methodology and Field Application. SPE/ISRM Rock Mechanics Conference. Irving, Texas; 2002.

[25] Nouri A, Vaziri H, Kuru E, Islam R. A comparison of two sanding criteria in physical and numerical modeling of sand production. J Pet Sci Eng 2006; 50:55-70.

[26] Kooijman AP, Halleck PM, de Bree P, Veeken CAM, Kenter CJ. Large-scale laboratory sand production test. SPE Annual Technical Conference and Exhibition. Washington, D.C.; 1992.

[27] Kooijman AP, van den Hoek PJ, de Bree P, Kenter CJ, Zheng Z, Khodaverdian M. Horizontal wellbore stability and sand production in weakly consolidated sandstones. SPE Annual Technical Conference and Exhibition. Denver, Colorado; 1996.

[28] Rasouli V, Evans B. A true triaxial stress cell to simulate deep downhole drilling condition. Australian Petroleum Production & Exploration Association Journal 2010:61-70.

[29] Holt RM, Brignoli M, Fjær E, Unander TE, Kenter CJ. Core damage effects on compaction behaviour. Rock Mechanics in Petroleum Engineering. Delft, Netherlands; 1994.

[30] Younessi A, Rasouli V, Wu B. Proposing a sample preparation procedure for sanding experiments. 2nd Southern Hemisphere International Rock Mechanics Symposium (SHIRMS). Sun City, South Africa; 2012.

[31] Nouri A, Vaziri HH, Belhaj HA, Islam MR. Sand-production prediction: a new set of criteria for modeling based on large-scale transient experiments and numerical investigation. SPE J 2006:227-37.

[32] Franklin JA, Vogler UW, Szlavin J, Edmond JM, Bieniawski ZT. Suggested methods for determining water content, porosity, density, absorption and related properties and swelling and slake-durability index properties: Part 1: Suggested methods for determining water content, porosity, density, absorption and related properties. Int J Rock Mech Min Sci & Geomech Abstr 1979; 16:143-51.

[33] Franklin JA. Suggested methods for determining the strength of rock materials in triaxial compression: Revised version. Int J Rock Mech Min Sci & Geomech Abstr 1983; 20:285-90.

[34] Bieniawski ZT, Bernede MJ. Suggested methods for determining the uniaxial compressive strength and deformability of rock materials: Part 1. Suggested method for determining

deformability of rock materials in uniaxial compression. Int J Rock Mech Min Sci & Geomech Abstr 1979; 16:138-40.

[35] Bieniawski ZT, Bernede MJ. Suggested methods for determining the uniaxial compressive strength and deformability of rock materials: Part 1. Suggested method for determination of the uniaxial compressive strength of rock materials. Int J Rock Mech Min Sci & Geomech Abstr 1979; 16:137.

[36] Younessi A, Rasouli V, Wu B. Numerical simulation of sanding under different stress regimes. The 46th US Rock Mechanics / Geomechanics Symposium. Chicago, IL; 2012.

[37] Willson SM, Moschovidis ZA, Cameron JR, Palmer ID. New model for predicting the rate of sand production. SPE/ISRM Rock Mechanics Conference. Irving, Texas; 2002.

[38] Tronvoll J. Experimental investigation of perforation cavity stability. The 33th U.S. Symposium on Rock Mechanics (USRMS), Santa Fe, NM; 1992.

[39] Fjær E, Holt RM, Horsrud P, Raaen AM, Risnes R. Petroleum related rock mechanics. 2nd ed: Elsevier Science; 2008.

[40] Detournay E, Fairhurst C. Two-dimensional elastoplastic analysis of a long, cylindrical cavity under non-hydrostatic loading. Int J Rock Mech Min Sci & Geomech Abstr 1987; 24:197-211.

[41] Risnes R, Bratli RK, Horsrud P. Sand Stresses around a wellbore. SPE J. 1982; 22:883-98.

[42] Sadd MH. Elasticity: Theory, Applications, and Numerics. 2nd ed: Academic Press; 2009.

[43] Younessi A, Rasouli V, Wu B. Experimental sanding analysis: Thick walled cylinder versus true triaxial tests. 2nd Southern Hemisphere International Rock Mechanics Symposium SHIRMS. Sun City, South Africa; 2012.

Figure 17 Lateral stresses coefficients for tangential stress.

Figure 18 Stress profile along line A-A for set 1 (top) and set 3 (bottom) of numerical simulations.

Table 1

Fluid Properties			
γ_{oil}	Fluid Weight density	7875.5	N/m^3
μ_{oil}	Fluid Dynamic viscosity	0.024	Pa.s
ν_{oil}	Fluid Kinematic viscosity	2.99E-05	m^2/s
Physical Properties			
ρ_b	Bulk density	1815	kg/m^3
ρ_g	Grain density	2500	kg/m^3
n	Porosity	0.274	-
k	Permeability	1.63E-13	m^2
Elastic Properties			
E	Young's modulus	7.65	GPa
ν	Poisson ratio	0.18	-
α	Biot's constant	1	-
Strength Parameters			
UCS	Uniaxial compressive strength	5.37	MPa
T_0	Tensile strength	0.7	MPa
Mohr-Coulomb Parameters			
C	Cohesion	1.47	MPa
ϕ	Internal friction angle	32.6	deg
Drucker-Prager Parameters			
d	Shear yield stress	3	MPa
β	Friction angle	52.8	deg
K	Flow stress ratio	0.8	-

Table 2

Test Number	σ_L MPa	σ_l MPa	σ_l/σ_L -	σ_a MPa	P_p MPa	Width deg	Max. depth mm
B1401	14	8	0.57	8	4	120	3.4
B1402	14	10	0.71	8	4	140	3.6
B1403	14	12	0.86	8	4	170	3.2
B1404	14	14	1.00	8	4	180	2.3
B1601*	16	6.4	0.40	6.4	3.2	105	4.9
B1602*	16	11.2	0.70	6.4	3.2	150	4.6
B1603*	16	16	1.00	6.4	3.2	180	4.4

* These tests were presented and discussed by the Authors in references [38, 39].

Figure 1

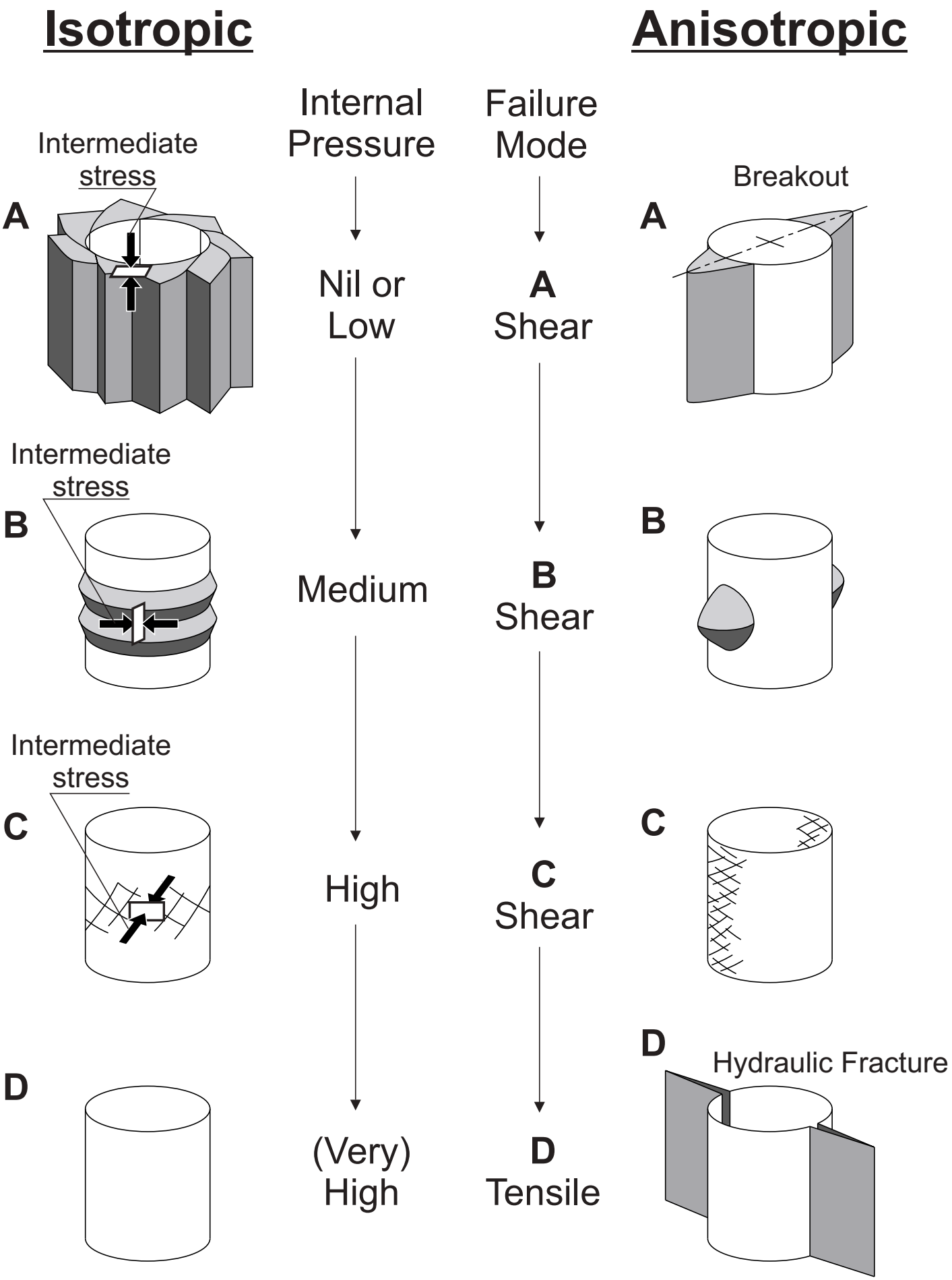
Isotropic
Anisotropic
Internal Pressure
Failure Mode
Intermediate stress
A
Nil or Low
A Shear
Breakout
A
Intermediate stress
B
Medium
B Shear
B
Intermediate stress
C
High
C Shear
C
D
(Very) High
D Tensile
D
Hydraulic Fracture

Figure 2

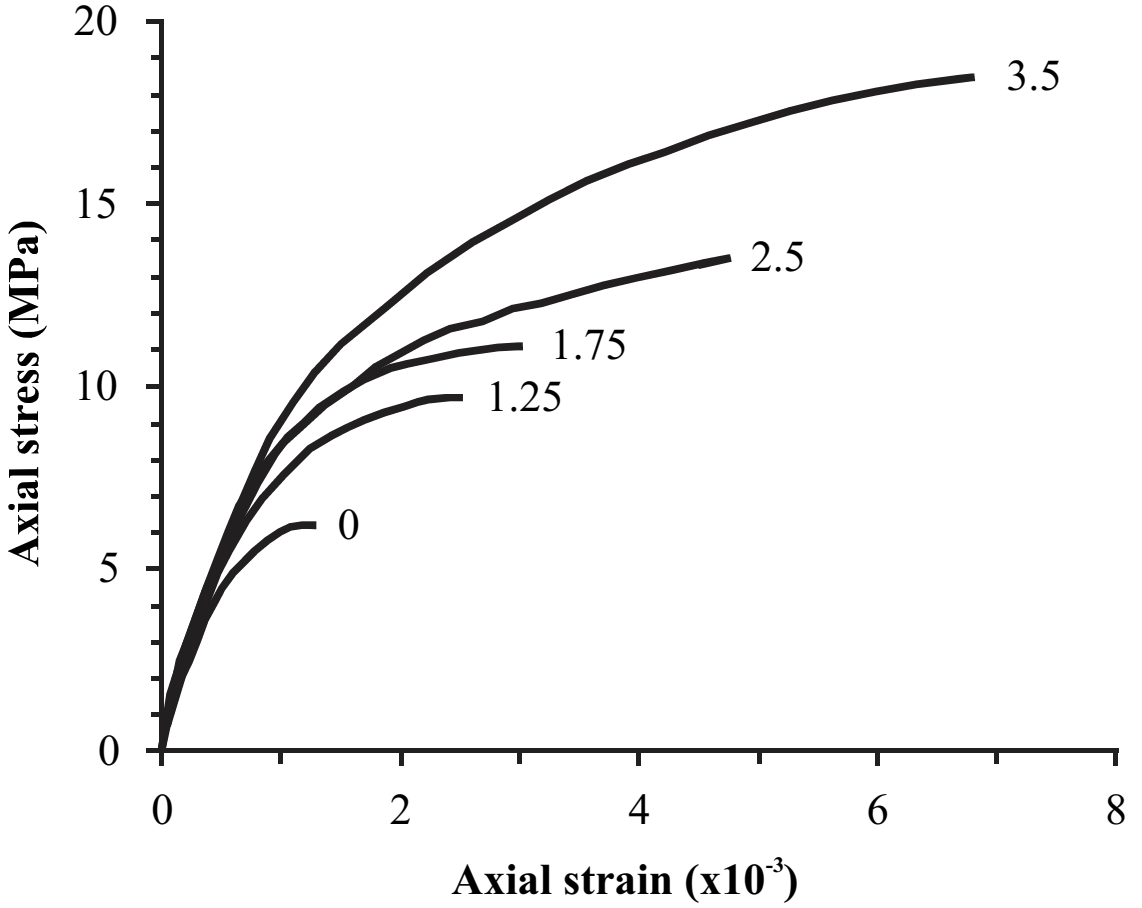
20
15
10
5
0
Axial stress (MPa)
3.5
2.5
1.75
1.25
0
0
2
4
6
8
Axial strain (x10-3)

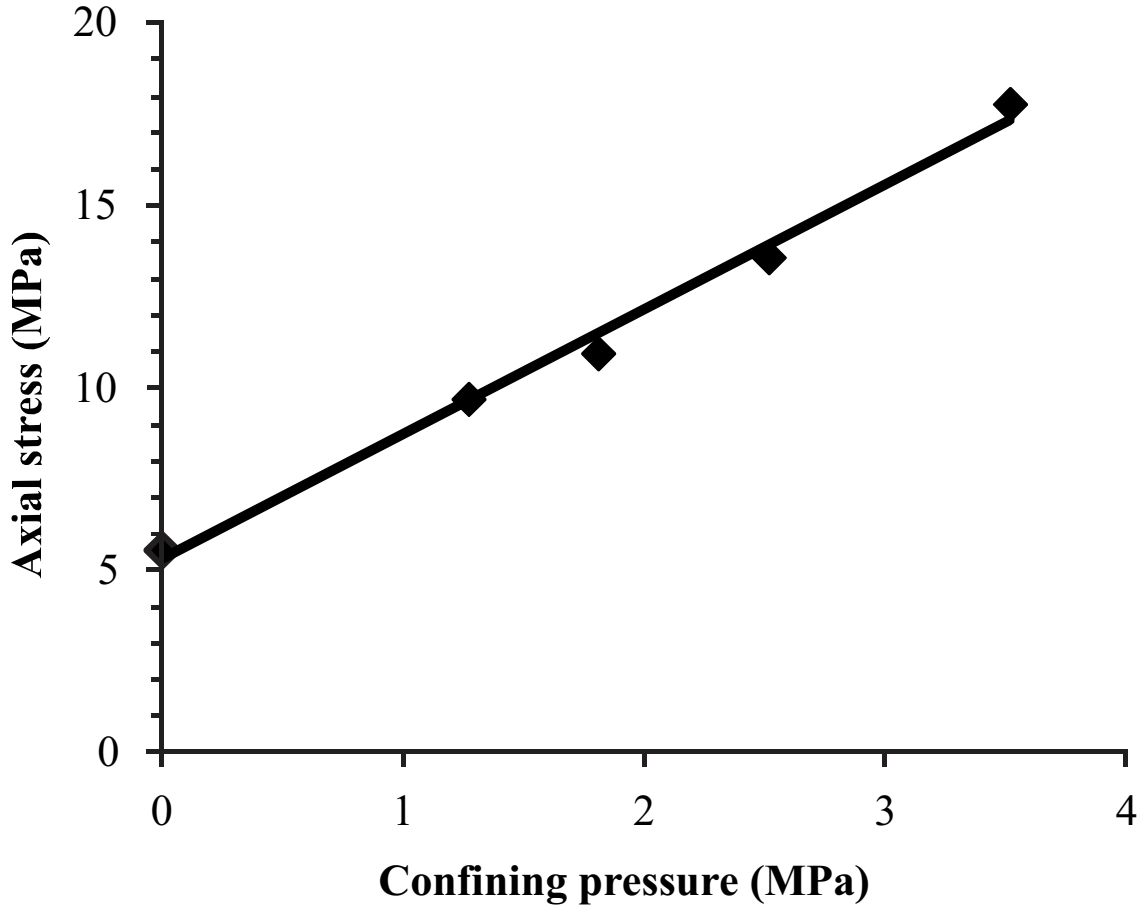
20
15
10
5
0
Axial stress (MPa)
0
1
2
3
4
Confining pressure (MPa)

Figure 3

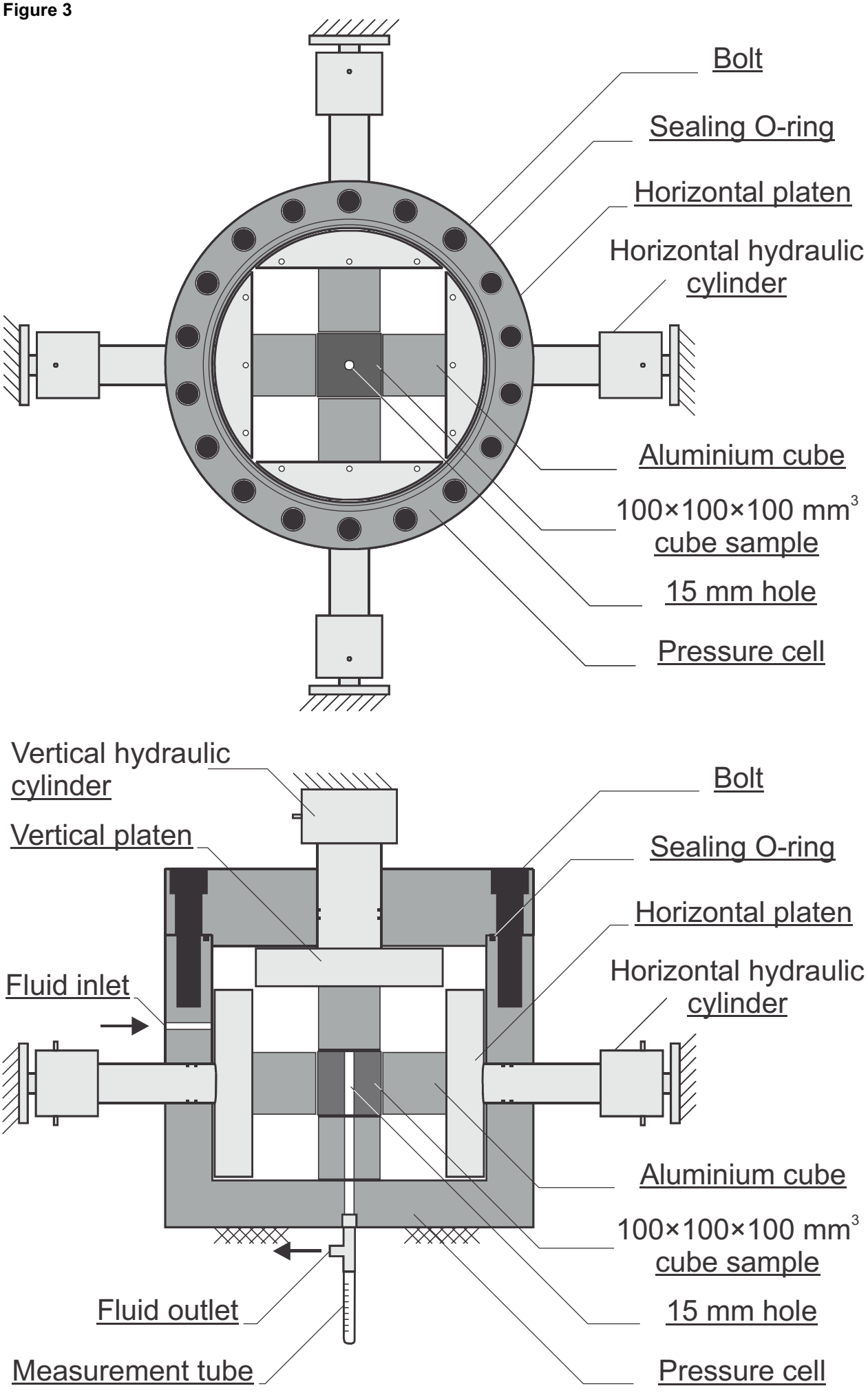
Bolt
Sealing O-ring
Horizontal platen
Horizontal hydraulic cylinder
Aluminium cube
100×100×100 mm3 cube sample
15 mm hole
Pressure cell
Vertical hydraulic cylinder
Vertical platen
Fluid inlet
Fluid outlet
Measurement tube

Figure 4

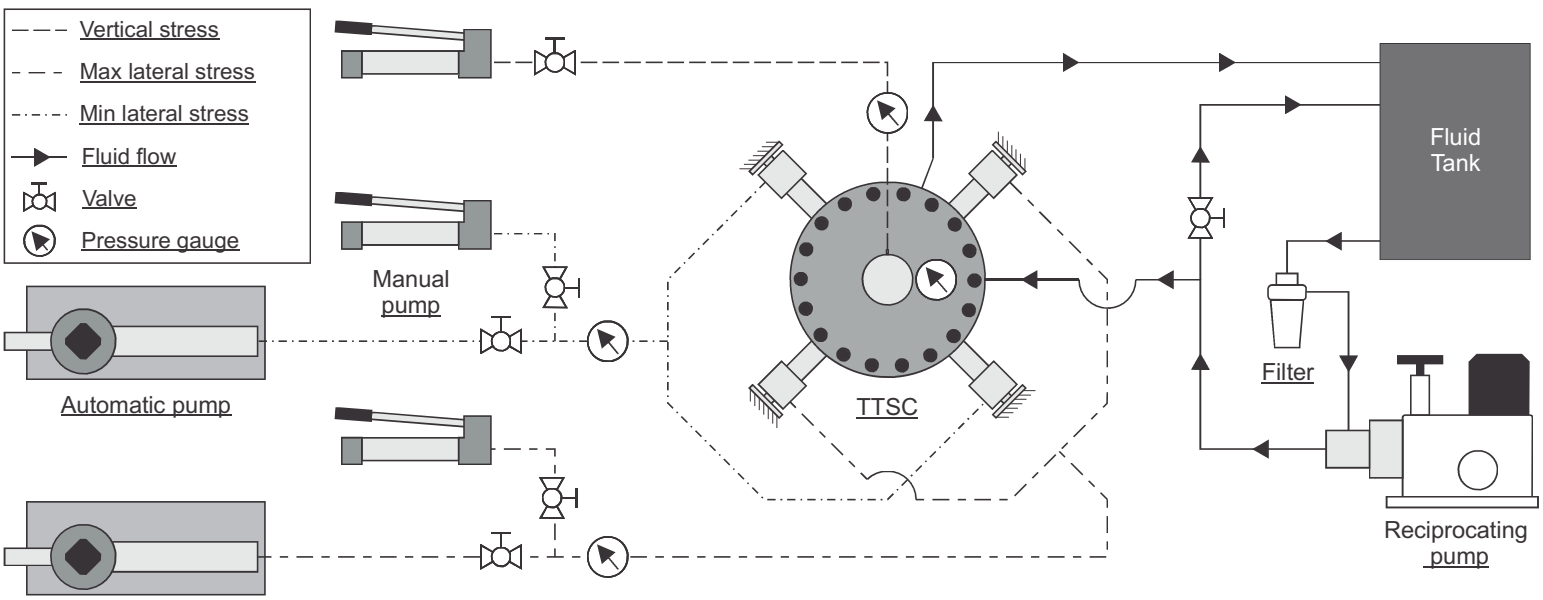
Vertical stress
Max lateral stress
Min lateral stress
Fluid flow
Valve
Pressure gauge
Manual pump
Automatic pump
TTSC
Fluid Tank
Filter
Reciprocating pump

Figure 5

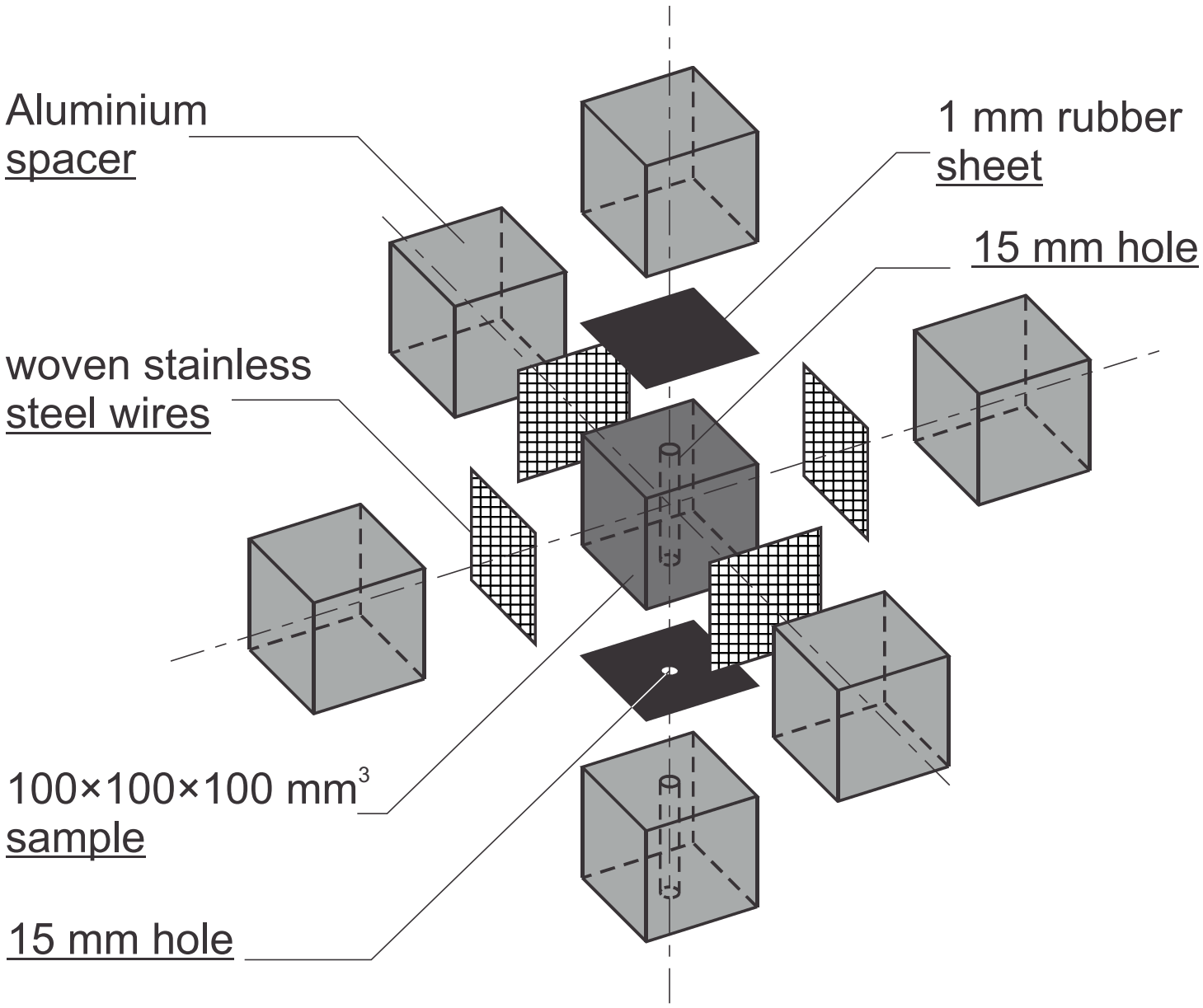
Aluminium spacer
1 mm rubber sheet
15 mm hole
woven stainless steel wires
100×100×100 mm3 sample
15 mm hole

Figure 6

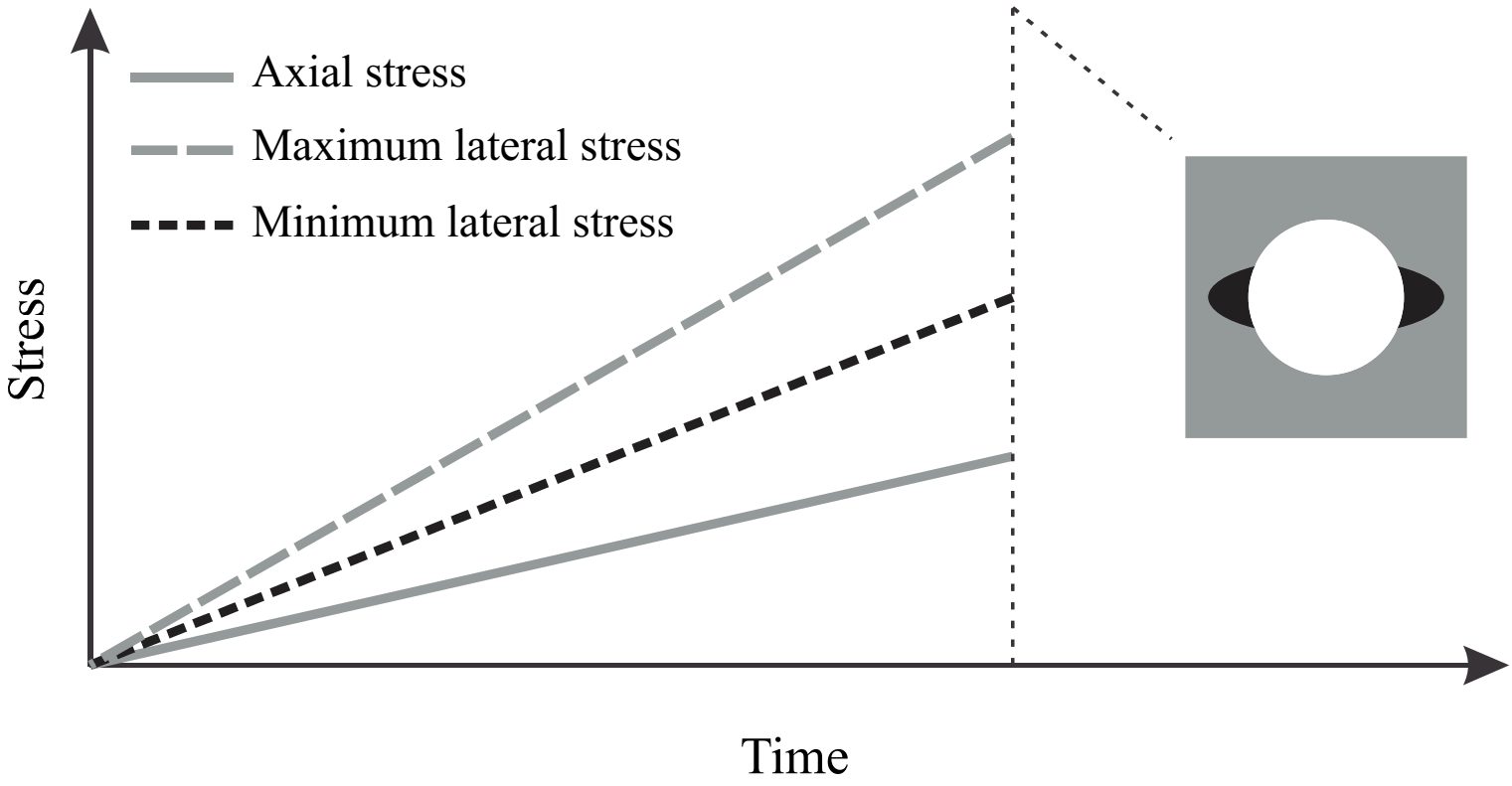
Axial stress
Maximum lateral stress
Minimum lateral stress
Stress
Time

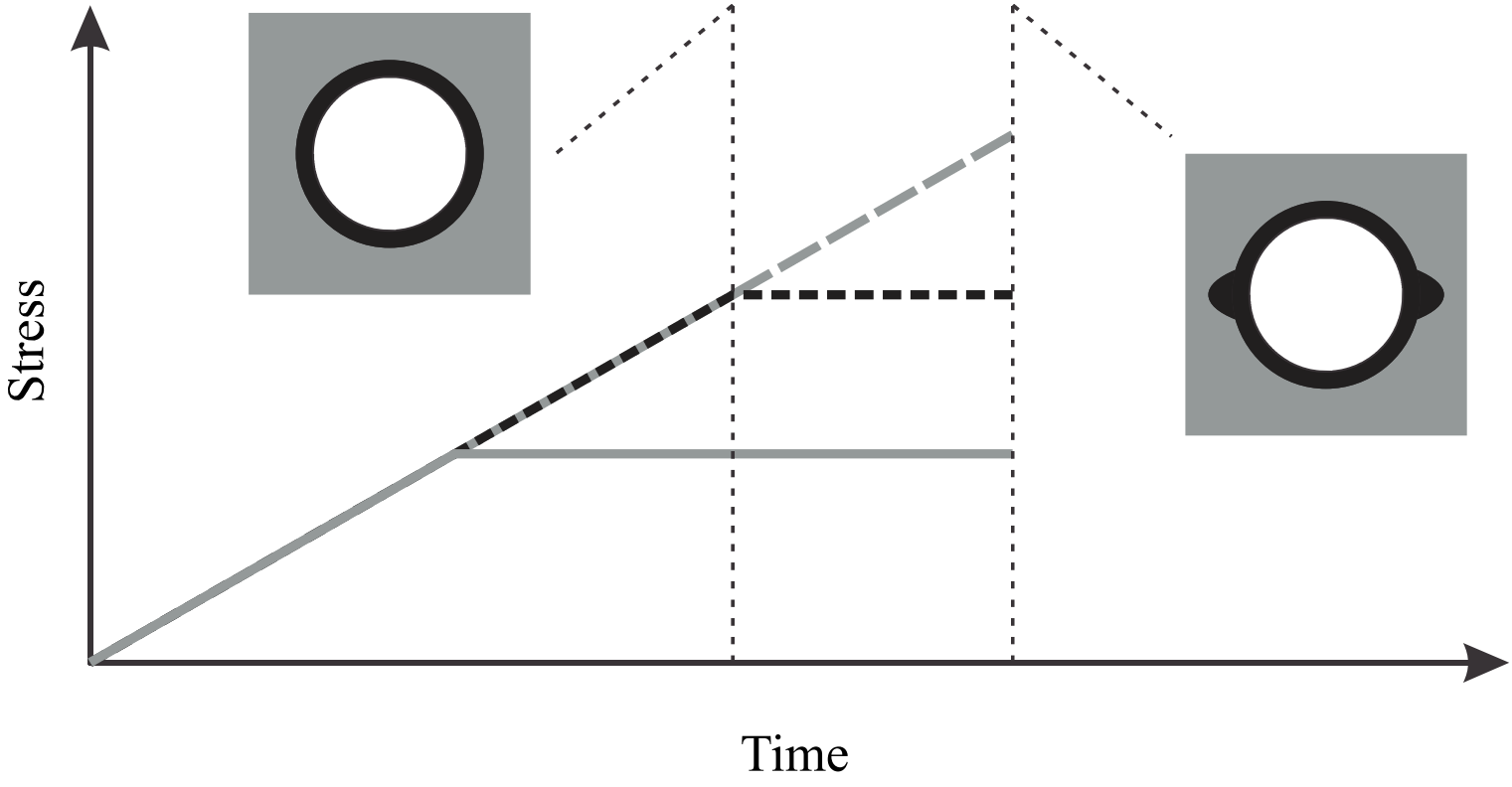
Stress
Time

Figure 7

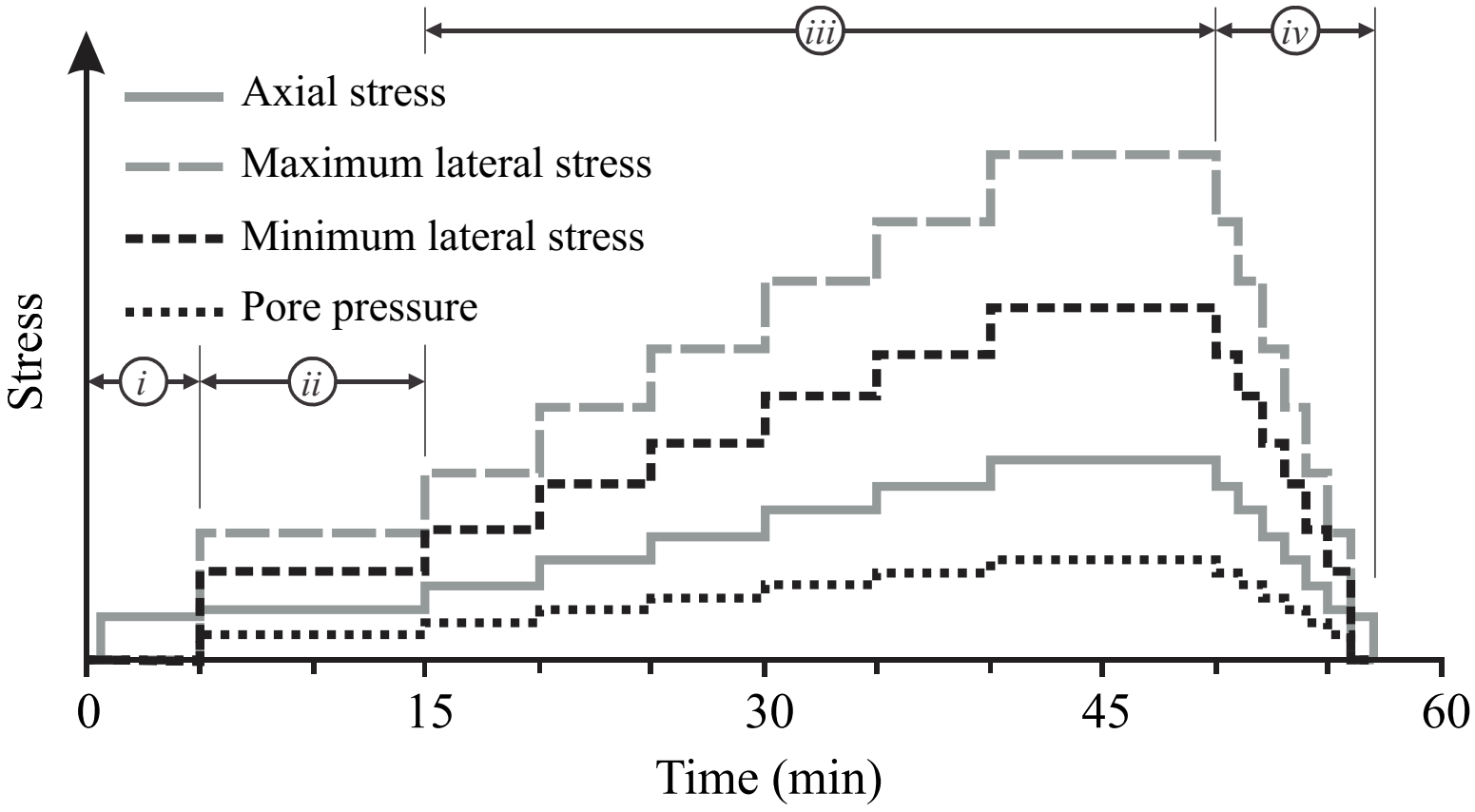
iii
iv
Axial stress
Maximum lateral stress
Minimum lateral stress
Pore pressure
i
ii
Stress
0
15
30
45
60
Time (min)

Figure 8

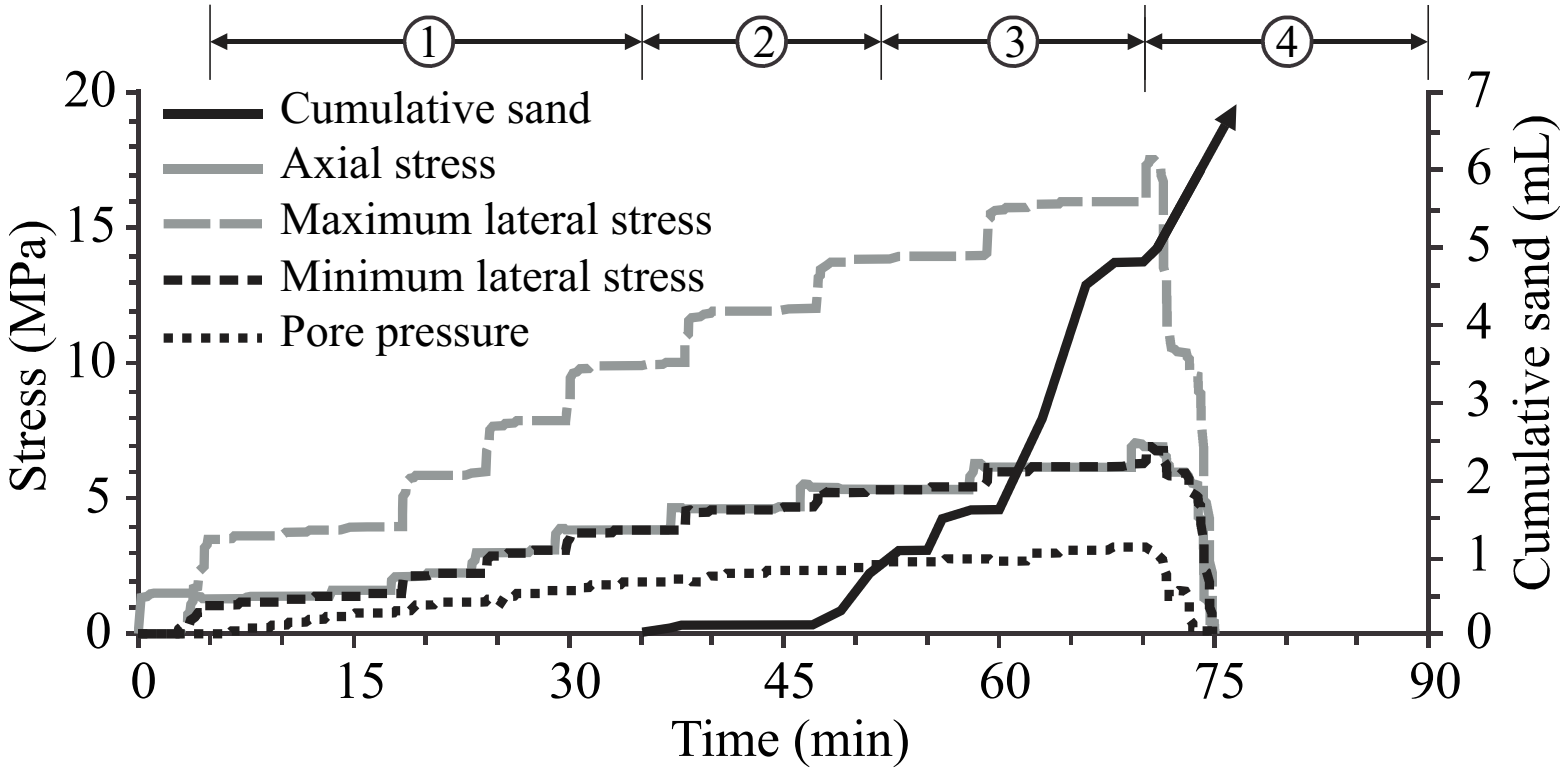
1
2
3
4
Cumulative sand
Axial stress
Maximum lateral stress
Minimum lateral stress
Pore pressure
Stress (MPa)
Cumulative sand (mL)
Time (min)
0
5
10
15
20
0
1
2
3
4
5
6
7
0
15
30
45
60
75
90

Figure 9

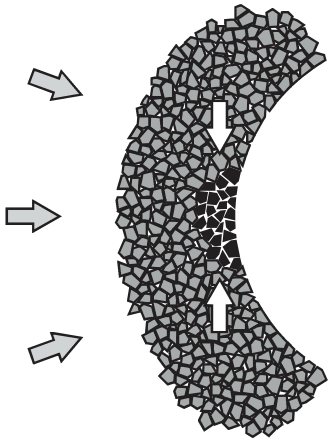

(1) Borehole wall yields in the direction of minimum lateral stress when the induced stresses around the borehole exceed the sandstone strength. However, the fluid flow is not strong enough to wash out the sand grains.

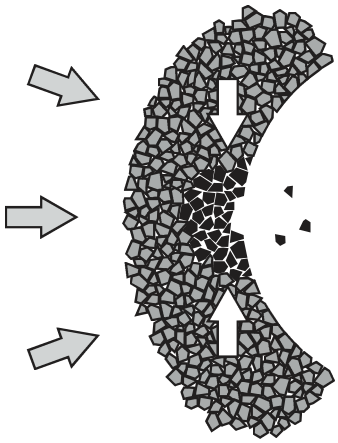

(2) Yield zone extended as the boundary stresses increased. The fluid flow is now strong enough to wash out the failed sands.

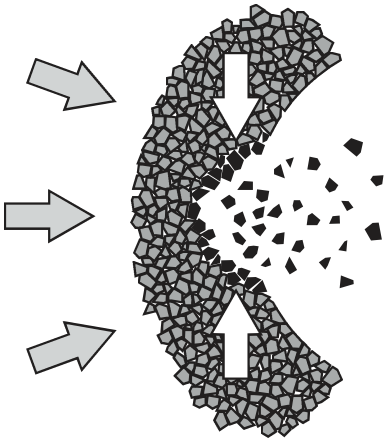

(3) Increase of boundary stresses results growing of the yield zone. large amount of sand are produced due to high flow rate. However, the borehole is stabilized after certain amount of sand is produced.

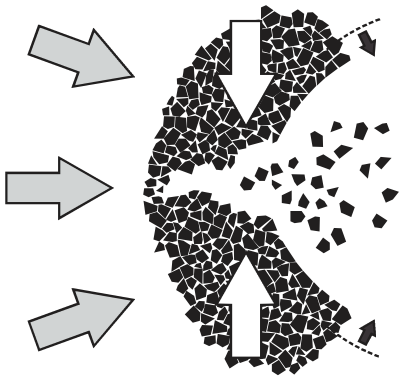

(4) The whole sample is yielded. Continuous sands are produced till the test is stoped. Large borehole wall deformations are observed.

Figure 10

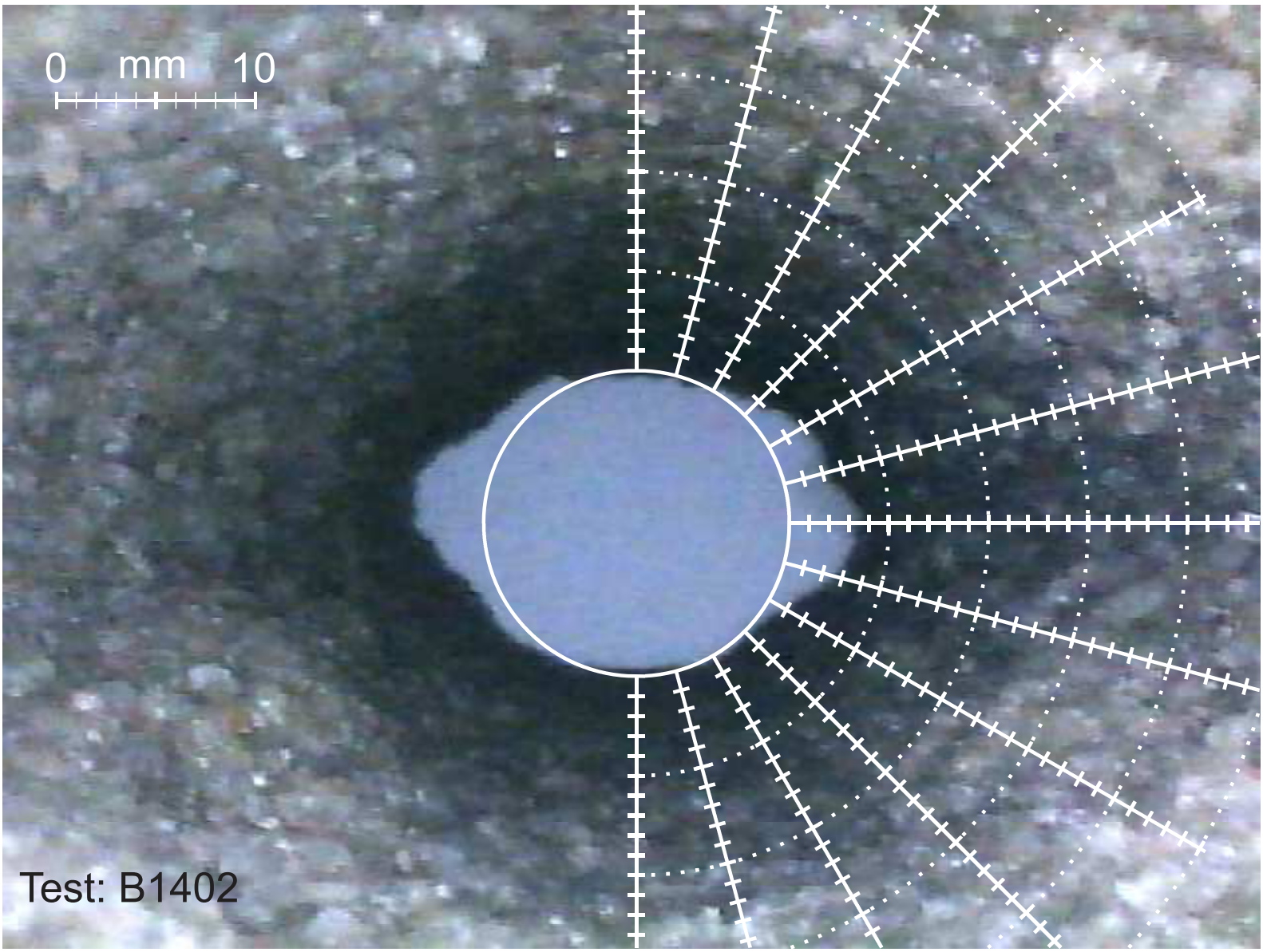

Figure 11

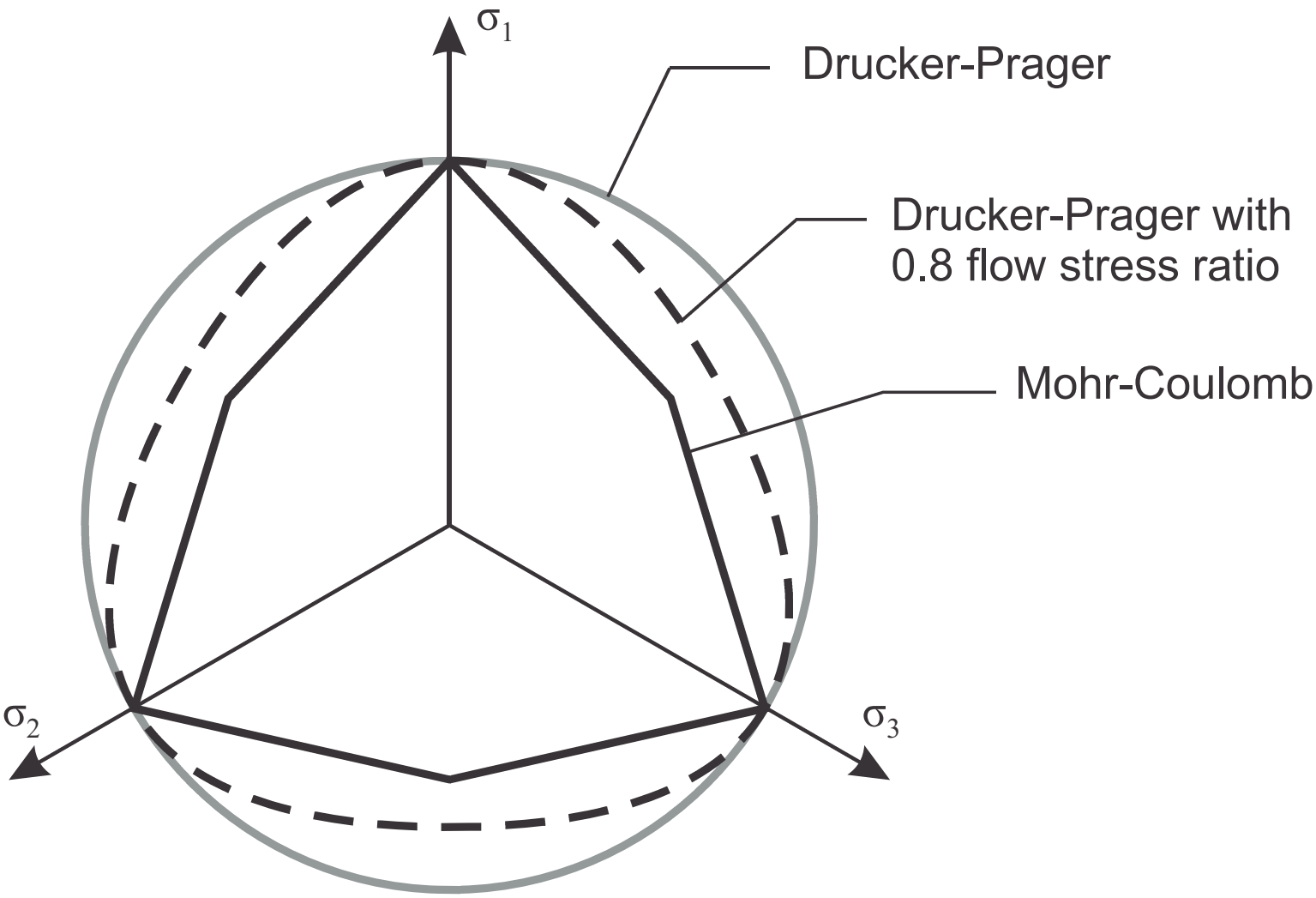
σ1
Drucker-Prager
Drucker-Prager with
0.8 flow stress ratio
Mohr-Coulomb
σ2
σ3

Figure 12

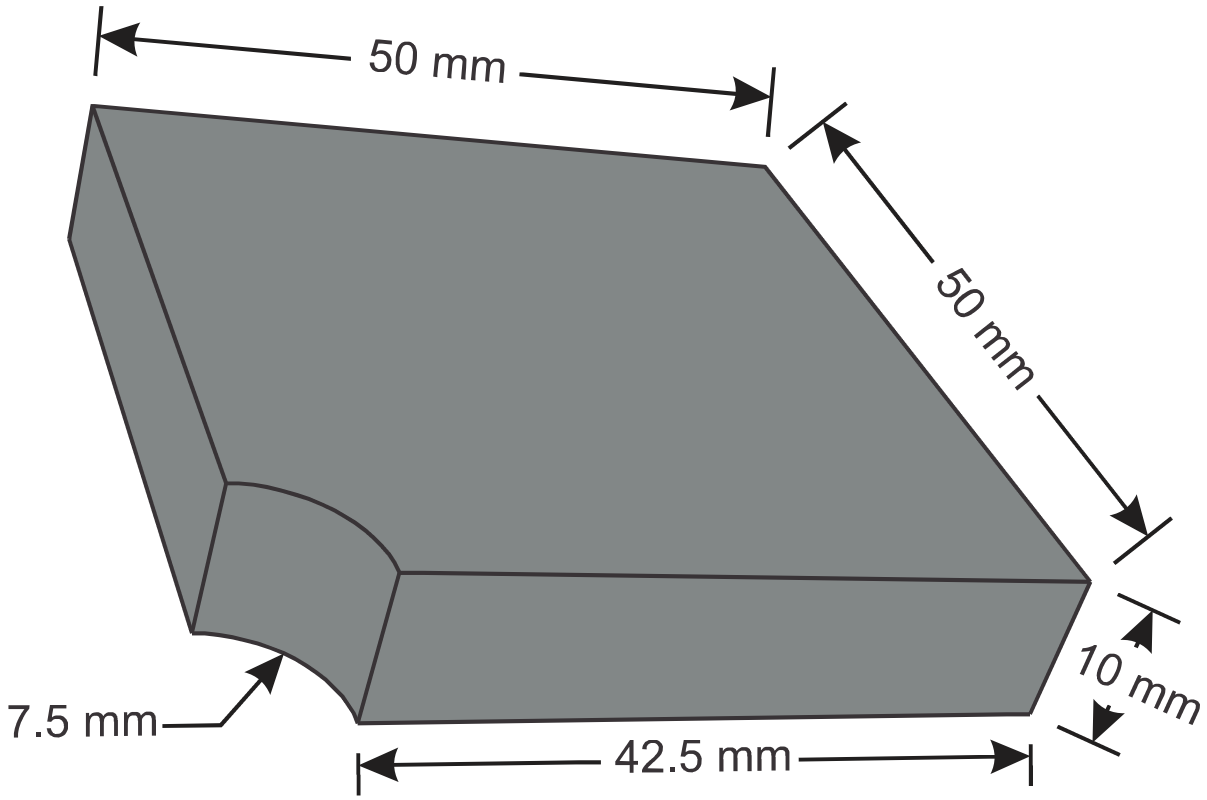
50 mm
50 mm
10 mm
7.5 mm
42.5 mm

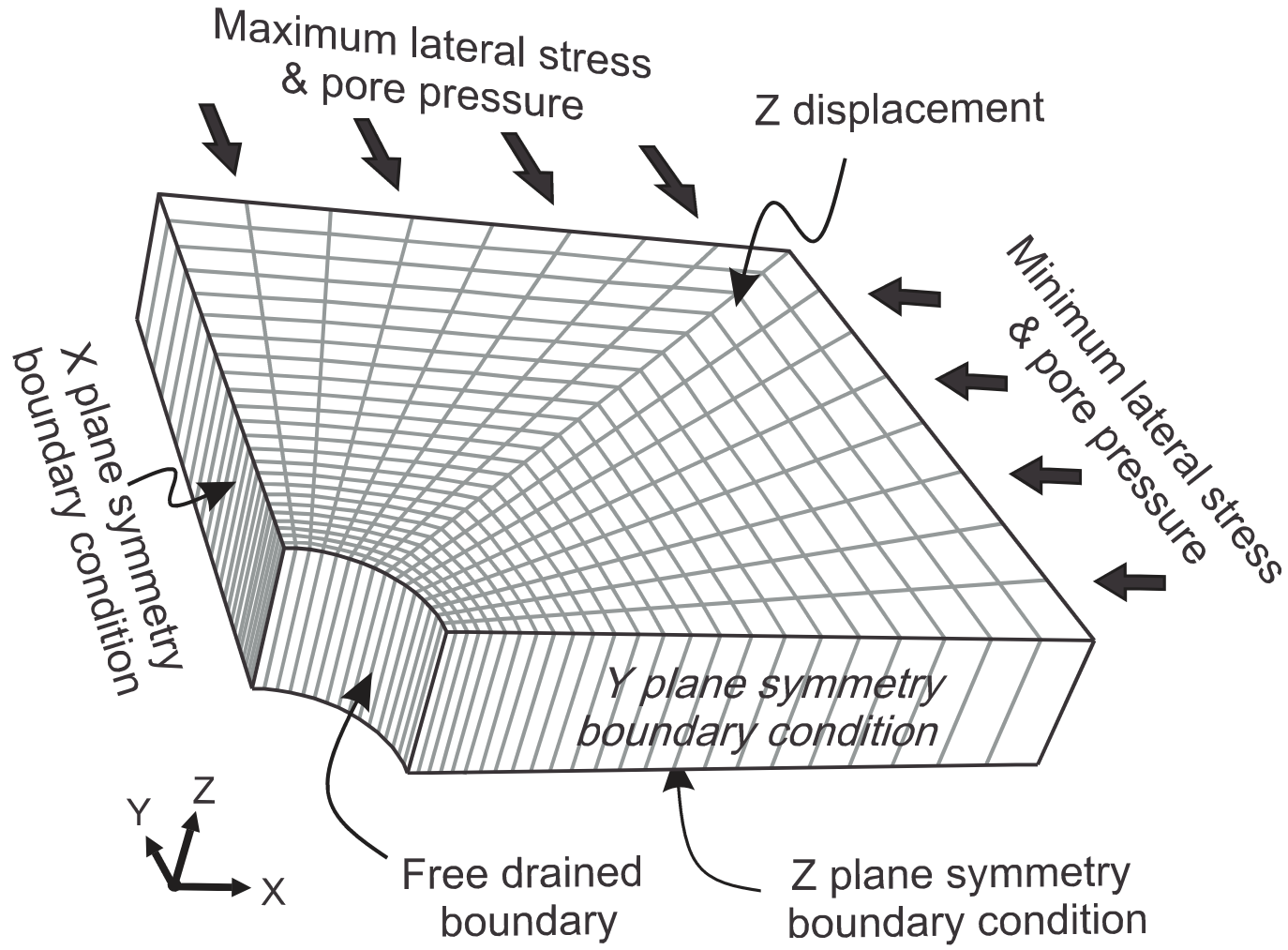
Maximum lateral stress
& pore pressure
Z displacement
Minimum lateral stress
& pore pressure
X plane symmetry
boundary condition
Y plane symmetry
boundary condition
Y
Z
X
Free drained
boundary
Z plane symmetry
boundary condition

Figure 13

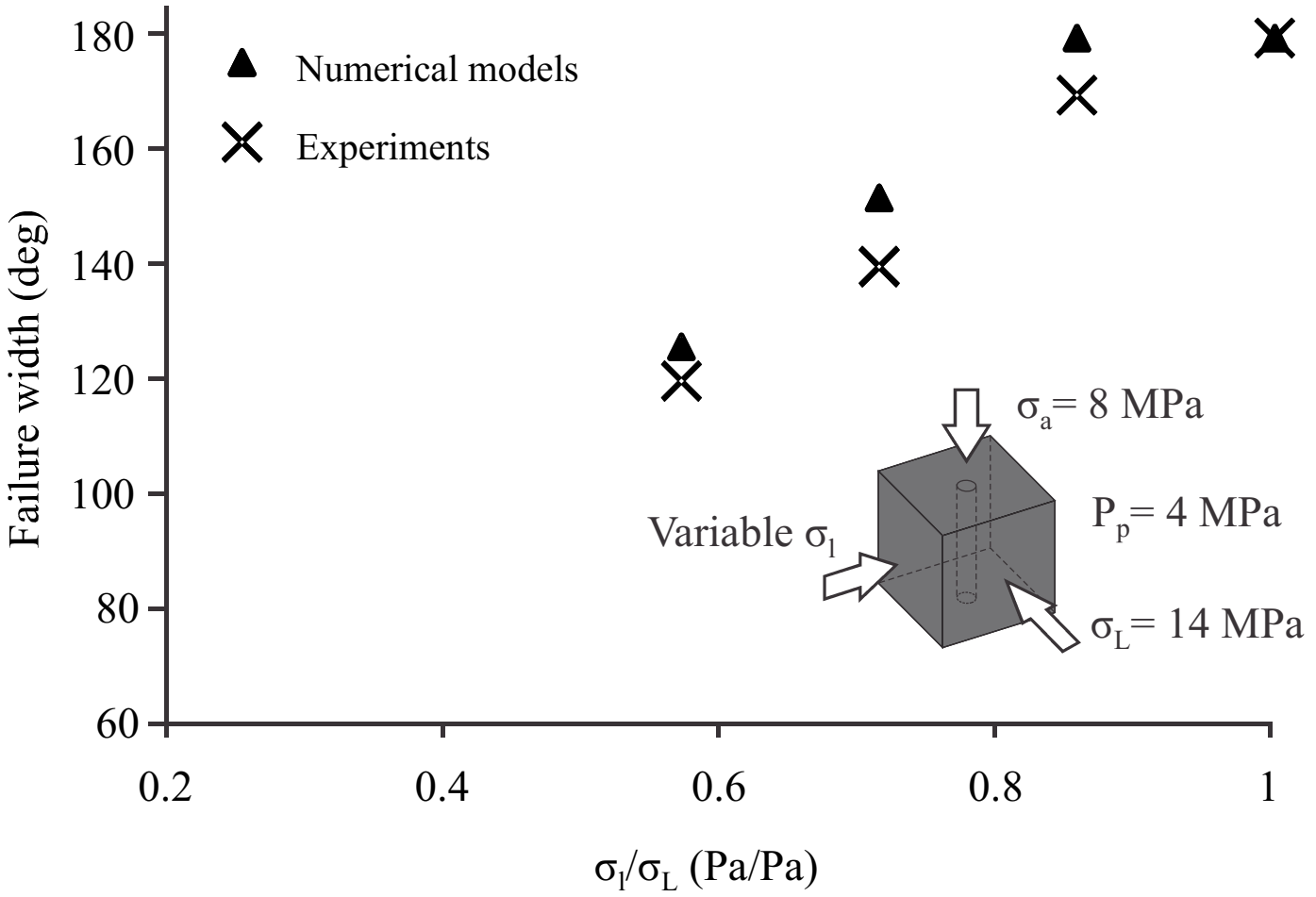
Numerical models
Experiments
Failure width (deg)
180
160
140
120
100
80
60
0.2
0.4
0.6
0.8
1
σl/σL (Pa/Pa)
σa= 8 MPa
Pp= 4 MPa
Variable σl
σL= 14 MPa

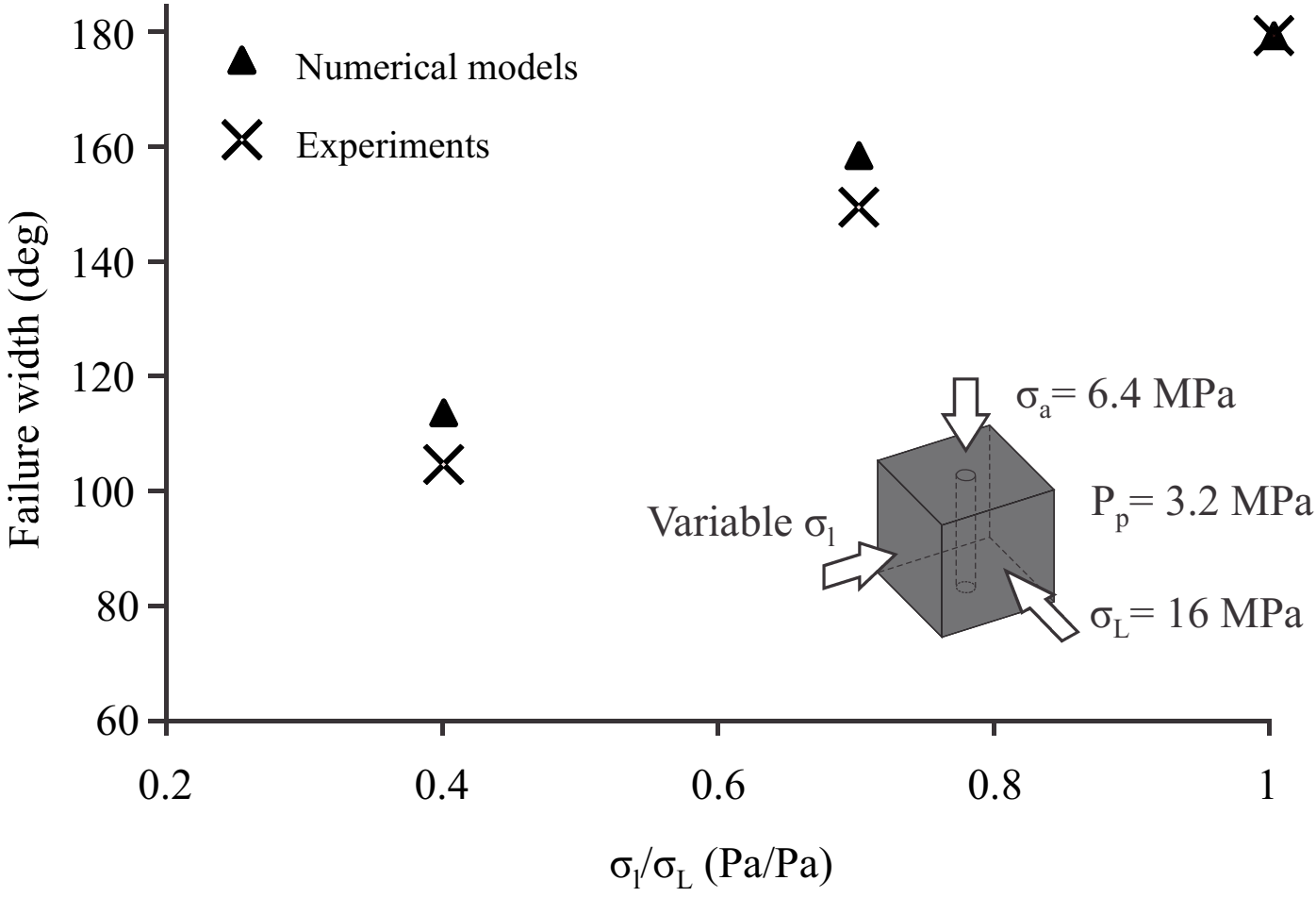
Numerical models
Experiments
Failure width (deg)
180
160
140
120
100
80
60
0.2
0.4
0.6
0.8
1
σl/σL (Pa/Pa)
σa= 6.4 MPa
Pp= 3.2 MPa
Variable σl
σL= 16 MPa

Figure 14

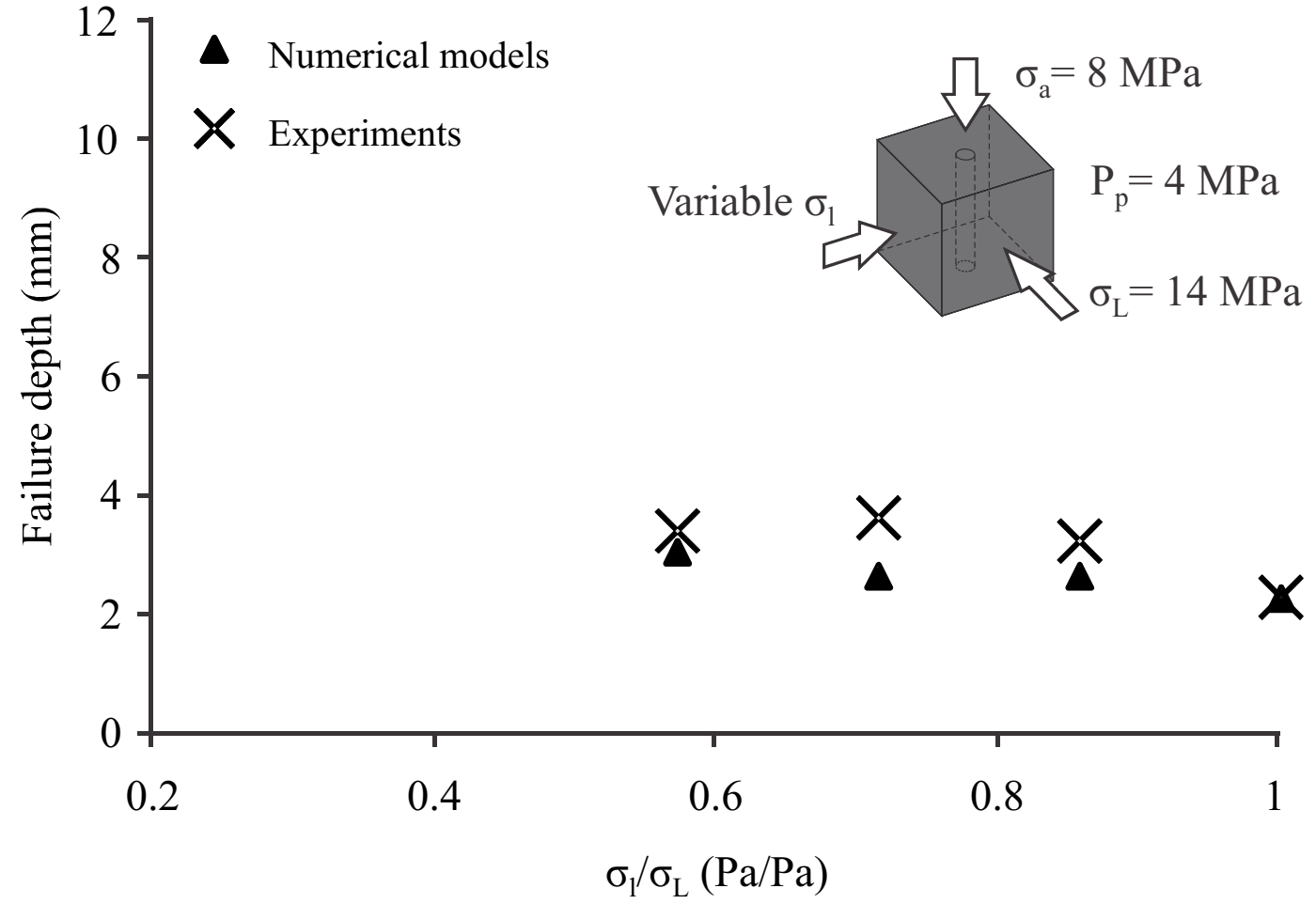
Numerical models
Experiments
σ_a= 8 MPa
P_p= 4 MPa
Variable σ_l
σ_L= 14 MPa
Failure depth (mm)
0
2
4
6
8
10
12
0.2
0.4
0.6
0.8
1
σ_l/σ_L (Pa/Pa)

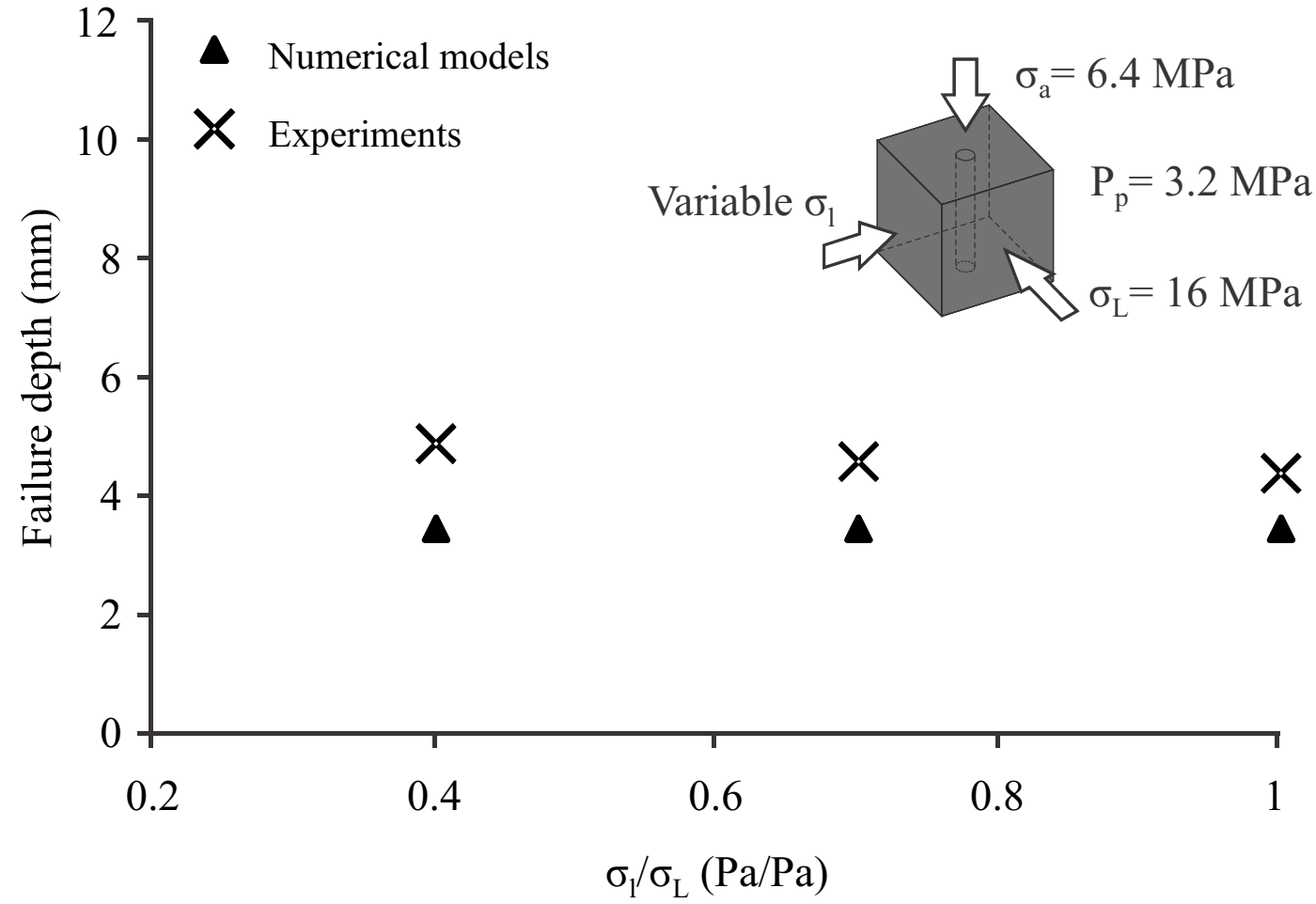
Numerical models
Experiments
σ_a= 6.4 MPa
P_p= 3.2 MPa
Variable σ_l
σ_L= 16 MPa
Failure depth (mm)
0
2
4
6
8
10
12
0.2
0.4
0.6
0.8
1
σ_l/σ_L (Pa/Pa)

Figure 15

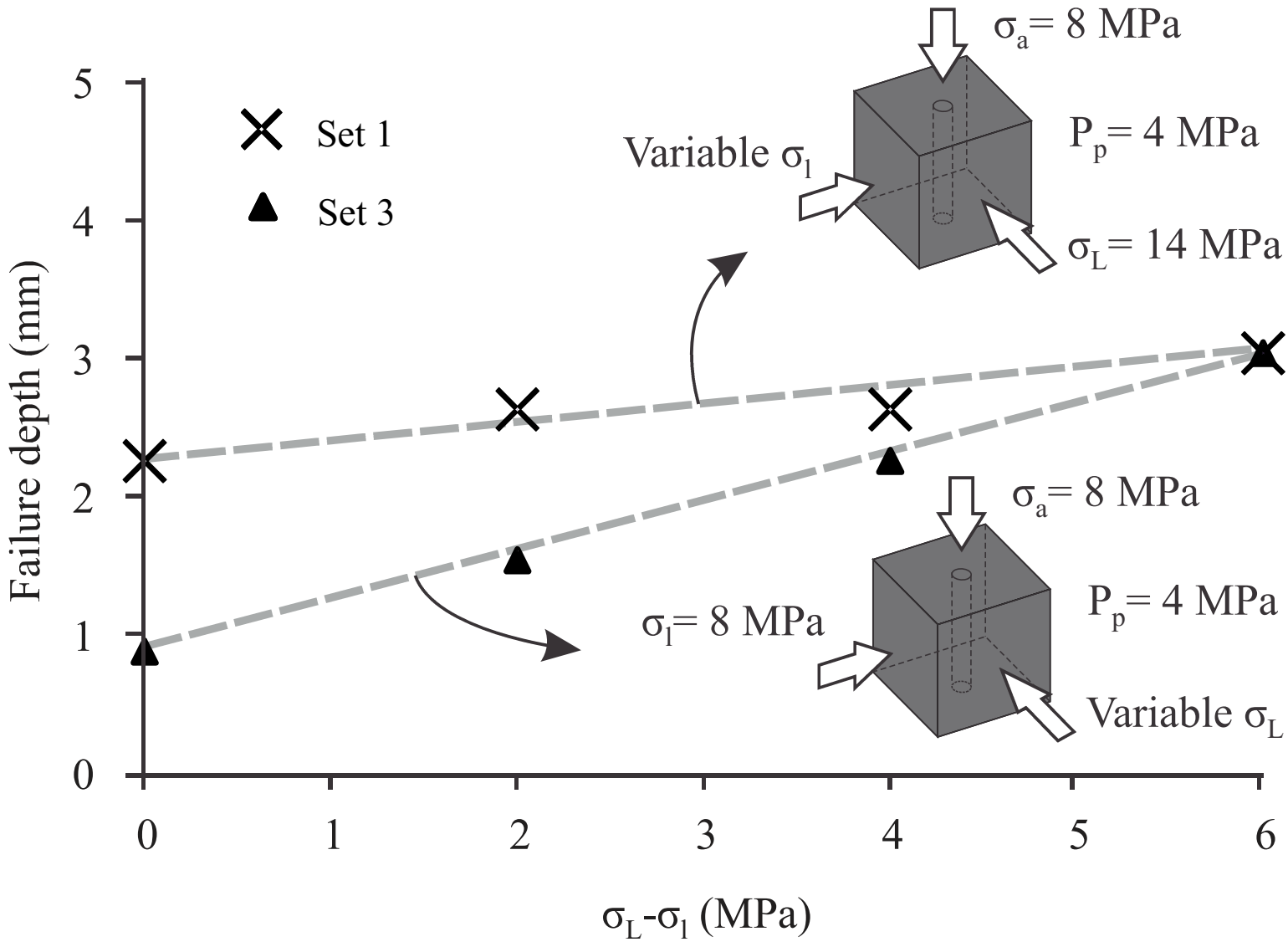
Failure depth (mm)
0
1
2
3
4
5
0
1
2
3
4
5
6
σL-σl (MPa)
Set 1
Set 3
σa= 8 MPa
Pp= 4 MPa
Variable σl
σL= 14 MPa
σa= 8 MPa
Pp= 4 MPa
σl= 8 MPa
Variable σL

Figure 16

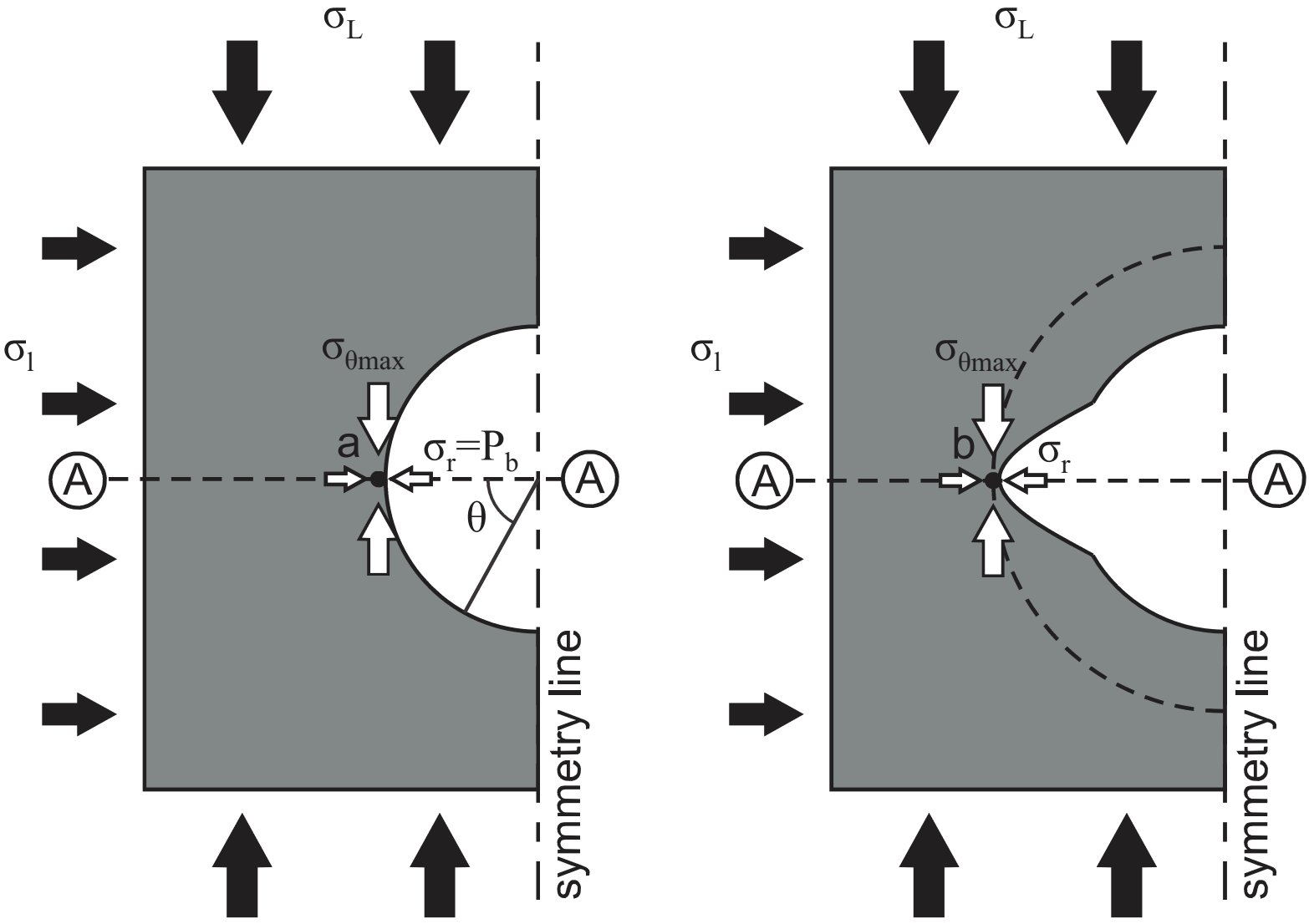
σL
σl
σθmax
a
σr=Pb
θ
A
A
symmetry line
σL
σl
σθmax
b
σr
A
A
symmetry line

Figure 17

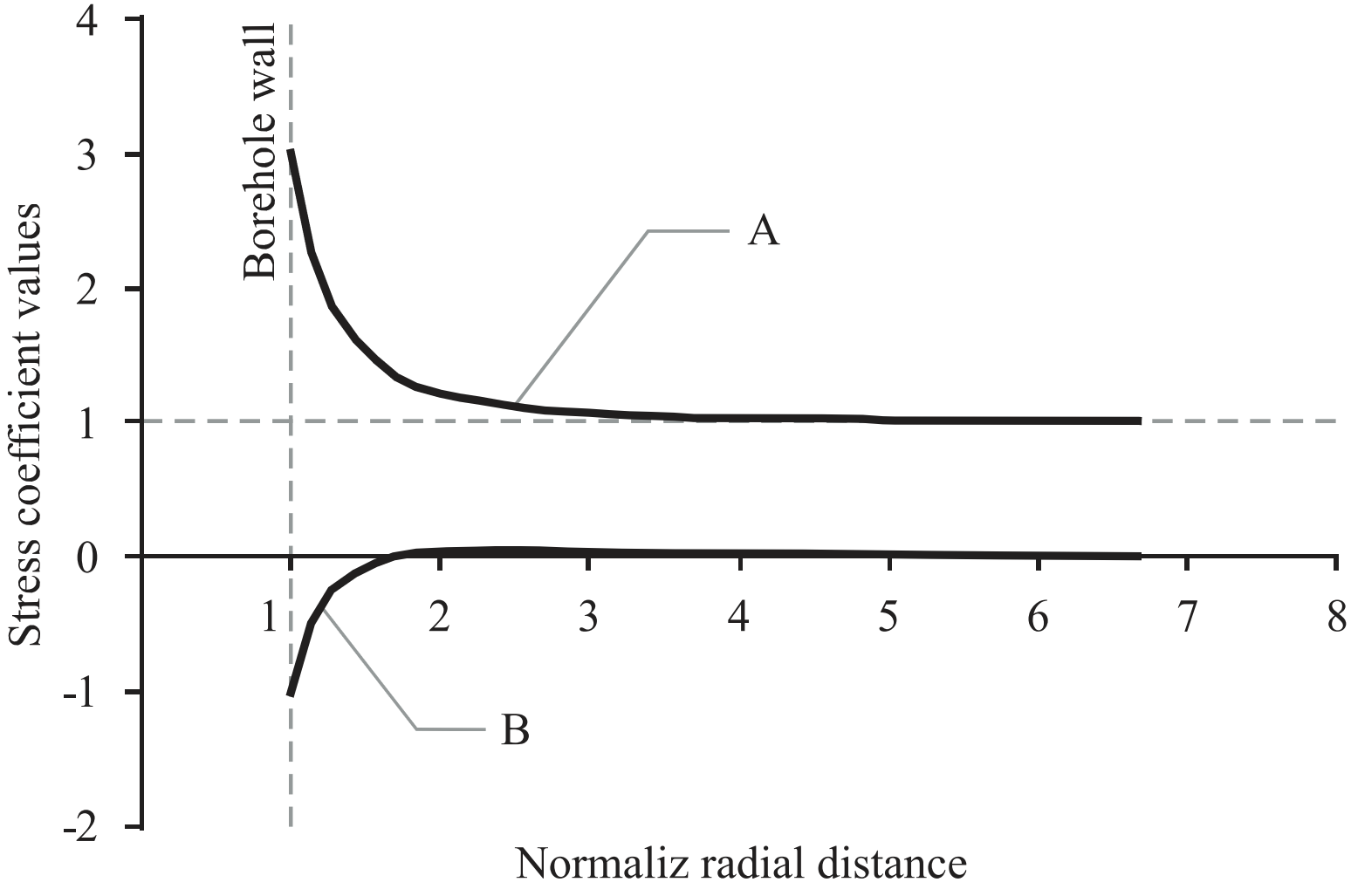
4
3
2
1
0
-1
-2
Stress coefficient values
Borehole wall
A
B
1
2
3
4
5
6
7
8
Normaliz radial distance

Figure 18

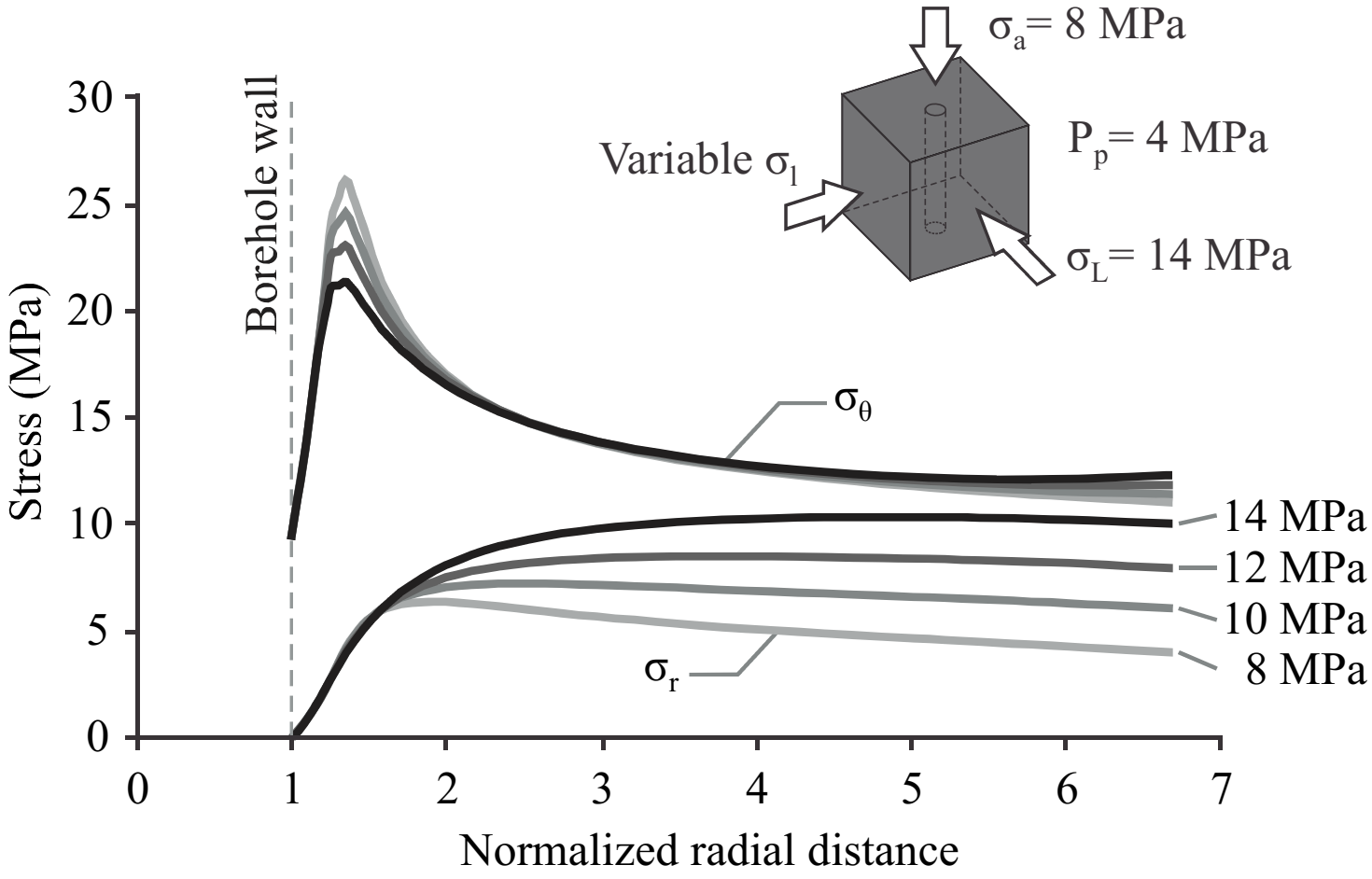
σa= 8 MPa
Pp= 4 MPa
Variable σl
σL= 14 MPa
Borehole wall
Stress (MPa)
σθ
σr
14 MPa
12 MPa
10 MPa
8 MPa
Normalized radial distance

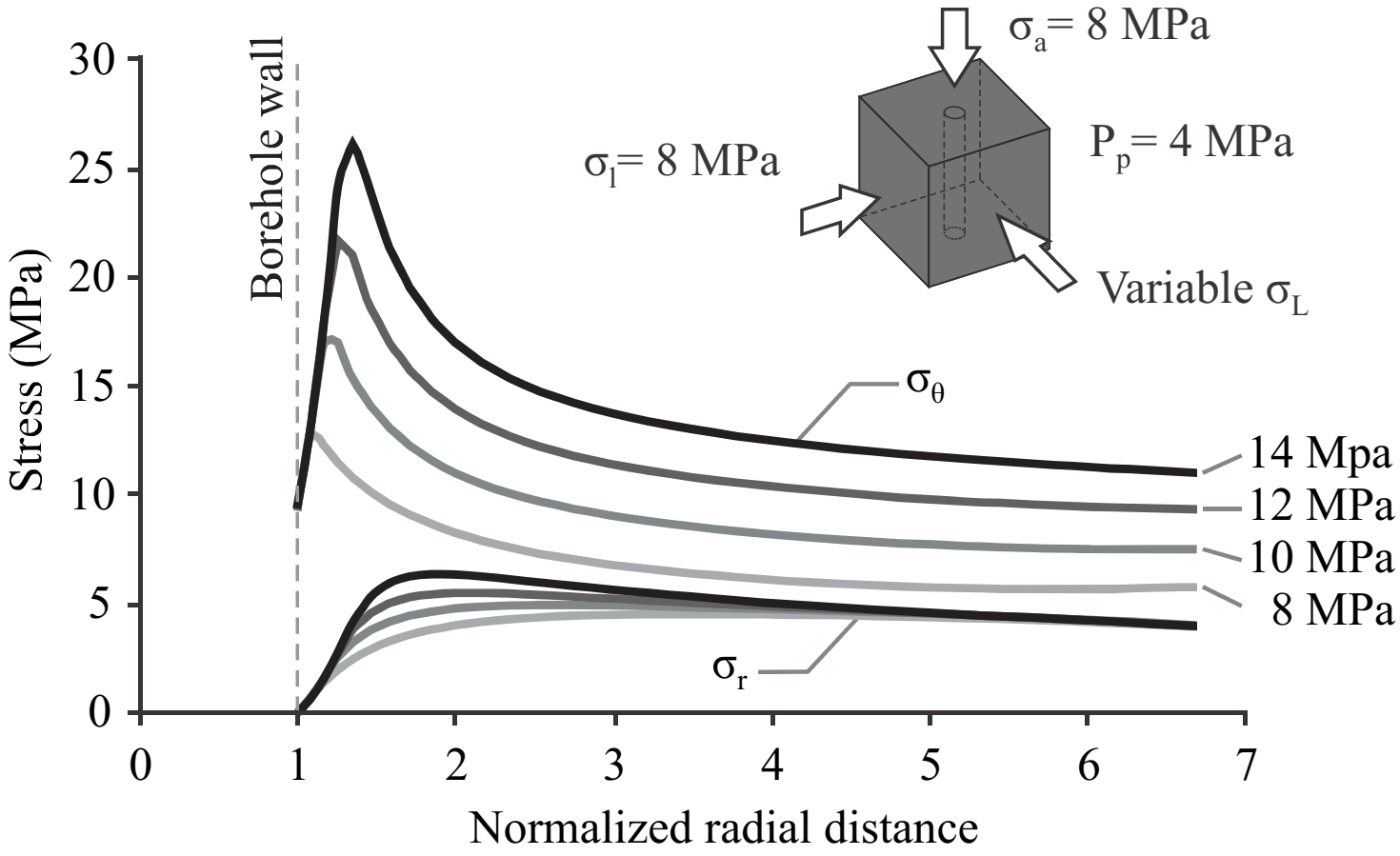
σa= 8 MPa
σl= 8 MPa
Pp= 4 MPa
Variable σL
Borehole wall
Stress (MPa)
σθ
σr
14 Mpa
12 MPa
10 MPa
8 MPa
Normalized radial distance